

**Computational exploration of the dual role of the phytochemical fortunellin: antiviral activities against SARS-CoV-2 and immunomodulatory abilities against the host**

Shivangi Agrawal<sup>1</sup>, Ekta Pathak<sup>2\*</sup>, Vibha Mishra<sup>1</sup>, Afifa Parveen<sup>1</sup>, Sunil Kumar Mishra<sup>3</sup>, Parameswarappa S Byadgi<sup>4</sup>, Shushil Dubey<sup>4</sup>, Ashvanee Kumar Chaudhary<sup>5</sup>, Vishwambhar Singh<sup>6</sup>, Rameshwar Nath Chaurasia<sup>7</sup>, Neelam Atri<sup>8</sup>, Rajeev Mishra<sup>1\*</sup>,

\* To whom correspondence should be addressed:

\*Rajeev Mishra, Ph.D.

Associate Professor in Bioinformatics, MMV,  
Institute of Science, Banaras Hindu University, Varanasi-221005, India.  
Tel: +91 9935338891, rajeev17@bhu.ac.in;

\* Ekta Pathak, Ph.D.

Bioinformatics Scientist (Freelance)  
Ph.D. in Bioinformatics, Banaras Hindu University  
Tel: +91 9651709839; ektavpathak@gmail.com

<sup>1</sup>Bioinformatics, MMV, Institute of Science, Banaras Hindu University. India

<sup>2</sup>Varanasi, Uttar Pradesh, India.

<sup>3</sup>Department of Pharmaceutical Engineering & Technology, IIT (BHU), India

<sup>4</sup>Faculty of Ayurveda, Institute of Medical Sciences, Banaras Hindu University, India

<sup>5</sup>Department of Otorhinolaryngology, Institute of Medical Sciences, BHU

<sup>6</sup>Department of ENT, IMS, BHU, India

<sup>7</sup>Department of Neurology, Institute of Medical Sciences, Banaras Hindu University, India

<sup>8</sup>Department of Botany, MMV, Banaras Hindu University, India

## Abstract

SARS-CoV-2 infection generates approximately one million virions per day, and the majority of available antivirals are ineffective against it due to the virus's inherent genetic mutability. This necessitates the investigation of concurrent inhibition of multiple SARS-CoV-2 targets. We show that fortunellin (acacetin 7-O-neohesperidoside), a phytochemical, is a promising candidate for preventing and treating COVID-19 and SARS by targeting multiple key viral target proteins, supporting protective immunity while inhibiting pro-inflammatory cytokines and apoptosis pathways, and protecting against tissue damage. Fortunellin is a phytochemical found in Gojihwadi Kwath, an Indian traditional Ayurvedic formulation with antiviral activity that has been shown to be effective in COVID-19 patients. The mechanistic action of its antiviral activity, however, is unknown. The current study comprehensively evaluates the potential therapeutic mechanisms of fortunellin in preventing and treating COVID-19 using molecular docking, molecular dynamics simulations, free-energy calculations, host target mining of fortunellin, gene ontology enrichment, pathway analyses, and protein-protein interaction analysis. Using computational approaches, we show that fortunellin reliably binds to key targets that are necessary for viral replication, growth, invasion, and infectivity, including Nucleocapsid (N-CTD) (-51.30 kcal/mol) and Replicase-dimer ( -45.91 kcal/mol), Replicase-monomer-NSP-8 binding site (-29.9 kcal/mol), Papain-like-protease (-29.60 kcal/mol), Nucleocapsid-NTD (28.46 kcal/mol), 2'-O-methyltransferase (-24.33 kcal/mol), Main-protease (-23.48 kcal/mol), Spike-RBD (-23.3 kcal/mol), Replicase-monomer at dimer interface (-23.27) kcal/mol, RNA-dependent-RNA-polymerase (-14.24 kcal/mol). Furthermore, we identify and evaluate the potential human targets of fortunellin and its effect on the SARS-CoV-2 infected tissues, including normal-human-bronchial-epithelium and lung cells, and organoids such as pancreatic, colon, liver, and cornea, using a computational network pharmacology approach. Thus, our findings indicate that fortunellin has a dual role: multi-target antiviral activities against SARS-CoV-2, as well as immunomodulatory capabilities against the host. In future, lab-based and clinical studies will be required.

**Keywords:** SARS-CoV-2, Fortunellin, Multi-target, Antiviral, Immunomodulation, Molecular dynamics simulation, MM-GBSA analysis, Enrichment analysis, Network Pharmacology,

## Introduction

SARS-CoV-2 causes COVID-19. COVID-19 individuals show respiratory symptoms, multi-organ failure, and inflammation, posing a major hazard to public health and life[1, 2] and, currently, treatment options are very limited. SARS-CoV-2 is an enveloped virus with a 30 kb RNA genome that encodes four structural proteins: 16 non-structural proteins [3]. These proteins help the virus multiply and survive in the host cell [4]. So targeting several viral proteins is an appealing way to reduce viral load. The Main-protease (Mpro) is a crucial enzyme in SARS-CoV-2 replication and transcription [5, 6], [5, 7]. Papain-like protease PLpro breaks down the translated polyproteins pp1ab and pp1a into their constituent proteins. PLpro inhibits the activation of the host's innate immune responses, allowing the coronavirus to invade the host cell [8],[9]. RNA-dependent RNA polymerase (RdRp) catalyzes the replication and transcription of the viral genome, making it essential for their survival [10]. Uridine-specific endoribonuclease (NendoU) and has been identified to be involved in RNA processing and is critical for the viral life cycle. Replicase of SARS-CoV-2 is vital for viral replication and transcription[11]. It undergoes dimerization, binds with RNA, interacts further with NSP8, and finally triggers the essential functions [12]. Helicase has both ATPase and helicase activity, as it unwinds the RNA helices in an ATP-dependent manner [13]. Another promising target is 2'-O-methyltransferase (nsp16). It participates in the Cap formation at the 5' end of the viral RNA which resembles the native mRNA of the host cells[14]. Spike glycoprotein drives the virus into the host cell and triggers immunological responses. The Spike glycoprotein has two subunits, S1 and S2, which mediate host cell interaction and membrane fusion. S1 contains the ACE2 receptor-binding domain (RBD) [15] [16]. Using an inhibitor on Spike-RBD can inhibit the spike's attachment to the ACE-2 receptor, preventing viral entrance. The Nucleocapsid N terminal binding domain (N-NTD) is essential for RNA binding and host infectivity[16] while the C-terminal domain (N-CTD) interacts with the viral membrane to bind the ribonucleoprotein complex [17]. Inhibiting this multifunctional Nucleocapsid protein can block both viral transcription and replication.

In this study, we have discovered a natural flavonoid O-glycoside compound, Fortunellin (PubChem ID: 5317385) as a potent inhibitor of 12 domains of the nine key protein targets of SARS-CoV-2 using Molecular Docking, MD simulations, and MM-GBSA analysis. Fortunellin is an Ayurvedic phytochemical found in Gojihwadi Kwath. Gojihwadi Kwath is antiviral and useful in COVID-19 management.[18-21]. But its antiviral activity's molecular mechanism is unknown. Aiming to inhibit the viral replication, growth, invasion, and infectivity, we tested the fortunellin binding to SARS CoV-2 key targets. A molecule is considered prospective in early-stage drug research if it can reliably dock to the targeted protein with high binding affinity and dynamic stability. We found that Fortunellin targets the virus's Mpro, PLpro, RdRp, NendoU, Replicase monomer at the NSP-8 binding site, Replicase dimer, Helicase, 2'-O-ribose Methyltransferase (MT), Spike-RBD, Nucleocapsid-NTD, and Nucleocapsid-CTD. Additionally, using free energy calculations and residue decomposition analysis we show that fortunellin masks the catalytically important residues of these targets. In addition, we have used the network pharmacology approach to detect the impact of fortunellin on normal human bronchial epithelial cells (NHBE) and lung cells, and organoids such as pancreatic, colon, liver, and cornea of the host system. The target host genes of fortunellin were shown to be involved in anti-inflammatory, immunomodulatory, and apoptotic pathways. The findings show that fortunellin has a dual role; multi-target antiviral activities against SARS-CoV-2, and immunomodulatory capabilities against the host. Given fortunellin's oral bioavailability and safety, this study could lead to the development of fortunellin as an orally active therapeutic against COVID-19 and SARS.

## **Methodology**

### **Molecular docking of fortunellin to SARS CoV-2 key targets**

The experimental structures of SARS-CoV-2 target proteins were retrieved from PDB[22]. (Supplementary table S1), and refined by adding missing atoms, polar hydrogen atoms, and Kollman charges to the residues and removing crystallographic water molecules using the dock prep tool[23].

The structure of fortunellin (PubChem ID: 5317385) was retrieved from NCBI PubChem[24]. Energy-minimization and geometry optimization of the structures was achieved using the Merck Molecular Force Field (MMFF94) using the Open Babel module of PyRx software [25]. Fortunellin was docked at the active binding pockets of the SARS-CoV-2 protein targets employing a grid-based docking method opting for a rigid protein receptor and flexible ligand docking protocol. The coordinates of the grid boxes were adjusted in x, y, and z dimensions according to the known active site of the proteins. Molecular docking was achieved using the AutodockVina software[26] . The structures were visualized and analyzed using UCSF Chimera 1.15[23].

### **Molecular Dynamics (MD) Simulation of fortunellin-SARS CoV-2 key target complex**

To validate the stability of the docked complex of fortunellin with Mpro, PLpro, RdRp, Endoribonuclease, Replicase (monomer as well as a dimer), Helicase, Methyltransferase, Spike, Nucleocapsid NTD, and CTD were subjected to molecular dynamics simulation for a timescale of 100 nanoseconds(ns) using GROMACS tool [27] and CHARMM 36m force field parameter set[28]. The web server SwissParam was used to generate the ligand topologies as well as the atomic charges of the ligands [29]. The MD simulations were conducted in a cubic water box solvated with TIP3P water molecules. To make the system electrically neutral, periodic boundary conditions were imposed in all directions, and Na<sup>+</sup>Cl<sup>-</sup> counter ions were added. The energy minimization of the systems was then achieved through 50,000 steps of steepest descents to alleviate any steric conflicts. After that, energy minimization for 100ps was followed by NVT and NPT equilibration. These systems were then submitted to MD simulation at 300K for 100 ns, with no restrictions on the residues, after they had been equilibrated in terms of pressure and density. Using a Berendsen thermostat, the system's temperature was kept at 300K throughout the experiment. The particle mesh Ewald method[30] was employed to account for the long-range electrostatic interactions, and the LINCS algorithm[31] was used, with a time step of 2fs to restrain bond lengths. The constant temperature and pressure (300K and 1bar) were maintained using a V-rescale thermostat[32] and Parrinello-Rahmanbarosta[33]. The production run was performed for 100ns with a leapfrog

integrator [34], and the coordinates were saved every ten picoseconds. A total of 10,000 frames were generated. MD trajectories were analyzed using the tools of GROMACS 2019.2. The plots were generated using Xmgrace [35]. To analyze the target-Fortunellin interactions, we used the representative snapshot of the most populated cluster obtained from the 70-100ns simulations using MD movie analysis of UCSF Chimera [23] package, and 2D interaction profiling was constructed using Maestro-12.4 (Schrödinger Release 2020–2: Maestro, Schrödinger, LLC, New York, NY, USA).

### **Binding free energy calculations of the SARS-CoV-2 targets and fortunellin complexes**

The MM-GBSA analysis was performed on AmberTools suite to investigate the free binding energies of the non-covalently bound protein and ligand complexes[36-39]. The ff99SB force field [40] is used to describe protein parameters. General Amber Force Field (GAFF)[41] with AM1-BCC charge model [42] is used for ligand molecule parameterization. Necessary input files (coordinates and topologies) were prepared with mbondi2 radii using LEaP. Minimization is performed in generalized Born implicit solvent models (igb=5) using the sander engine. For Free Energy calculation the following equation is used:  $\Delta G(\text{bind}) = \Delta G(\text{complex}) - [\Delta G(\text{receptor}) + \Delta G(\text{ligand})]$ .

From the 100ns MD simulation run a total of 1,000 snapshots were extracted, starting from the frame 7000 up to 10000 with an interval of 3 snapshots. Each component of the total free energy was estimated using the bonded, electrostatic, and van der Waals interactions as well as polar and non-polar solvated free energies. Furthermore, we also performed per-residues energy decomposition analysis to evaluate the energy contribution of each residue to the total energy.

### **Assessment of pharmacokinetic and pharmacodynamics features**

To predict the drug-likeness the comparative pharmacokinetic attributes like absorption, distribution, metabolism, and excretion (ADME) and other important pharmacological properties

(physicochemical properties, lipophilicity, water-solubility, and drug-likeness) of Fortunellin ADMETlab 2.0 [43] and pkCSM[44] servers were used. Furthermore, toxicity parameters like mutagenicity (AMES mutagenesis), hepatotoxicity, cytotoxicity, minnow toxicity, etc. of fortunellin were also predicted.

### **Prediction of upregulated host gene targets of fortunellin in Covid19 infected cells/organoids**

We predicted the targets of Fortunellin using the similarity ensemble approach[45] and the swiss target prediction tool[46]. Next, the differentially expressed (DE) gene lists specific to human cells/tissues/organoids including human NHBE cells (GSE147507), lung cells (GSE147507), pancreatic organoids (GSE151803), colon organoids (GSE148696), liver organoids (GSE151803), and cornea organoids (GSE164073) were downloaded from the Enrichr library “Covid-19\_Related\_Gene\_Sets\_2021”. Using Venn diagram (<http://bioinfogp.cnb.csic.es/tools/venny/>), we identified the tissue-specific gene targets of fortunellin which were upregulated after infection with Covid-19.

### **Functional enrichment analysis**

The identified host gene targets of fortunellin were further analyzed for its enriched biological processes, molecular functions, and cellular components utilizing the Enrichr tool [47] and bar plots were generated using the Appyters present in the Enrichr tool [47]. To obtain statistically significant results, the cut-off p-value used was less than 0.05 (p-value <0.05).

### **Protein-Protein Interaction Analysis, module detection, and pathway analysis**

Furthermore, the Cytoscape stringApp plugin [48] was used to investigate the protein-protein interaction network of fortunellin's target genes. With a confidence score of 0.4, we added 100 neighbor genes to the network. The expression of the integrated genes was investigated for its upregulation in Covid-19 infected cells/organoids using Enrichr library “Covid-19\_Related\_Gene\_Sets\_2021”. Using Cytoscape's MCODE plugin [49], we identified the network module. MCODE detects clusters that are highly interconnected within a network. Furthermore, we

used Cytoscape's cytohubba plugin's [50] maximum clique centrality (MCC) approach to determine the important (HUB) genes that were also targeted by fortunellin. Finally, we used the KEGG database [51] to identify the top five metabolic pathways of these modules to ascertain fortunellin's mode of action in the corresponding cell/organoids.

## Results

### Fortunellin targets 12 active pockets of nine key proteins of SARS-CoV-2

We have found that Fortunellin, a phytochemical derived from the Ayurvedic (Indian traditional medicine) formulation Gojihwadi, has multitargeting potential against SARS-CoV-2. Fortunellin showed a reliable negative binding energy (docking score) against the 12 ligand binding sites of nine key protein targets, including the virus's Mpro (-9.1kcal/mol), Papain-like protease (PLpro) (-9.0kcal/mol), RdRp (-9.0kcal/mol), NendoU (-8.9kcal/mol), Replicase monomer (NSP8 binding site) (-7.4 kcal/mol), Replicase mono Replicase dimer (-8.3 kcal/mol), Helicase (-10.4 kcal/mol), 2'-O-Methyltransferase (-9.8 kcal/mol), S-RBD (-7.8 kcal/mol), N-NTD (-8.2 kcal/mol), and N-CTD (-9.9 kcal/mol) (figure 1, Supplementary table S2). Furthermore, to evaluate the reliability and stability of docked complexes, each of the 12 fortunellin-SARS-CoV-2 target complexes was subjected to a 100ns MD simulation, producing 1.2  $\mu$ s of molecular trajectory data for analysis.

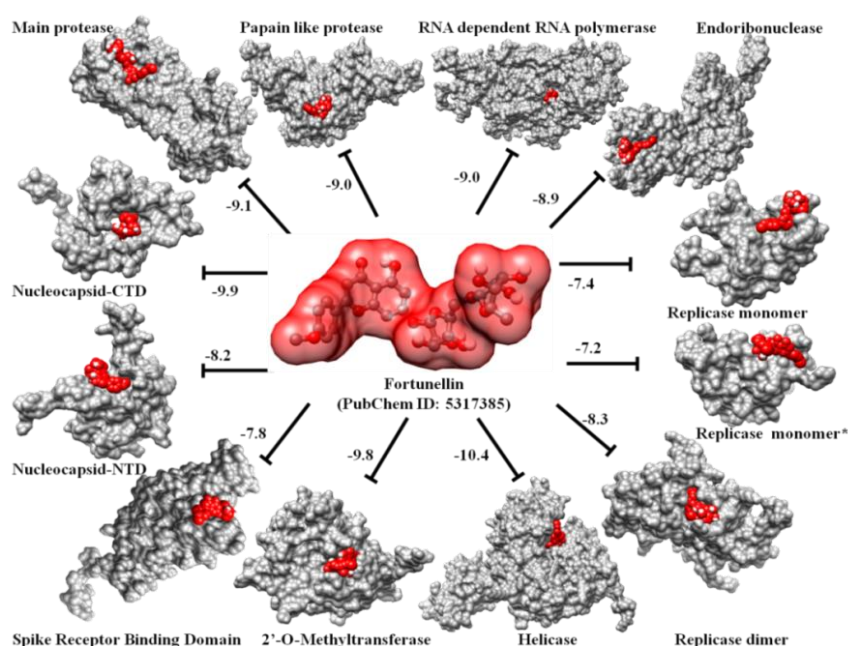


**Figure1. Molecular docking of fortunellin to SARS CoV-2 targets.** The surface view of the SARS-CoV-2 protein targets is depicted in grey. Fortunellin is displayed as surface view, and depicted in red colour. The values indicate the binding energy (Kcal/mol).



## **Molecular Dynamics (MD) simulation and MMGBSA analysis of fortunellin-Main protease complex**

To validate the stability of the docked complex of fortunellin-Mpro (figure 1), we performed a 100ns MD simulation. As a result, we observed a stable backbone conformational state with an average RMSD value of  $0.22 \pm 0.06$  nm (figure 2 (I-A)), suggesting the interaction stability. To decipher the structure compactness, the Rg value was computed (figure 2 (I-B)). The steady value ranging between 2.22 to 2.28 nm indicated that the protein is stably folded, stabilized, and has achieved a compact structure. The minimum distance analysis between the fortunellin and the Mpro was observed to be stabilized at ~0.18 nm throughout the trajectory indicating its stable interaction with the binding site residues (figure 2 (I-C)). To address local changes along the protein chain, RMSF of the residues of the fortunellin-M<sup>pro</sup> complex were analyzed. We found that the catalytic dyad HIS41-CYS145 residues were stably masked by the Fortunellin throughout the MD simulations (figure 2 (I-D)). Fortunellin-Mpro complex exhibited an average of five hydrogen bonds throughout the simulation (figure 2 (I-E)). Furthermore, we analyzed the fortunellin- Mpro interactions using the representative snapshot of the most populated cluster obtained from the last 30 ns MD trajectory simulations. We found polar interactions between Thr24, Thr25, Thr26, His41, Thr45, Ser46, Ser144, His164, Gln189, Thr190, and Gln192 residues of the main protease and fortunellin. In addition, fortunellin showed non-polar interactions with Leu27, Val42, Cys44, Cys145, Met165, Leu167, Pro 168, Val186, and Ala191.

The catalytic activity of the main protease is mainly mediated by a His-Cys catalytic dyad (His41 and Cys145) [52, 53]. Our results showed that fortunellin interacts with the catalytic dyad residues His41 and Cys145 that marks the unavailability of main protease to participate in polyprotein cleavage. Also, the formation of four H-bond pairs with Thr26, His41, Thr45, and Gln192 and charged interactions with Glu166, Asp187 and Arg188 provides extra stability to the docked complex (figure 2 (I-F)). In addition, the residues Gly143, Ser144, and Cys145 serve as the oxyanion

hole, are also considered important in drug designing as their blocking helps disrupt both substrate recognition and stabilization of the intermediate in the proteolytic reaction [6].

Furthermore, we calculated the binding free energy of fortunellin-Mpro complex using MMGBSA analysis and found a reliable  $\Delta G_{\text{bind}}$  value of -23.4878 kcal/mol with a standard deviation of  $\pm 7.5613$  kcal/mol (figure 2 (I-G), table 1). The binding of fortunellin at the active site of protein is predominantly stabilized by gas-phase interaction energy ( $\Delta G_{\text{gas}}$ ) and Vander Waal interaction energy ( $\Delta G_{\text{VDWAALS}}$ ) as indicated by figure 2 (I-G). To further quantify the contribution of binding pocket residues to the molecular interaction of fortunellin the free energy decomposition per residue was employed. Residue decomposition analyses revealed the key residues that stabilized this complex, which included Thr24, Thr25, Thr26, Leu27, His41, Cys44, Thr45, Ser46, Met49, Cys145, Met165, Glu166, Asp187, Arg188, Gln189 and Gln192 (figure 2 (IH)). This is consistent with the reports [54-56] that noted these residues as key players in ligand interactions with Mpro. Thus, fortunellin targeting Mpro may be considered a potential blocker of the viral replication during the Covid-19 infection.

### **MD simulation and MMGBSA analysis of fortunellin-papain-like protease complex**

In fortunellin-PLpro complex was stabilized with an average RMSD value of 0.23 nm in the 100ns MD trajectory (figure 2 (II-A)). It was also evident from the stabilized Rg value of the complex (figure 2 (II-B)). The lower degree of fluctuation with its consistency throughout the simulation indicates the greater compactness and rigidity of a system. The minimum distance between the PLpro and fortunellin was found to be stable with a distance of ~0.20 nm throughout the 100ns trajectory and suggests its occupancy in the pocket (figure 2 (II-C)). RMSF analysis of active site residues, especially the catalytic triad residues Cys111-His272-Asp286 of Plpro revealed low fluctuations within the complex with only a few peaks inferring to stabilize complex formation (figure 2 (II-D)). We observed three to four H-bonds during 100ns simulation which are sufficient enough to settle and block the space in the cleft and ultimately block the functionality of the target

(figure 2 (II-E)). In addition, to analyze the PLpro-fortunellin interactions, we used the representative snapshot of the most populated cluster obtained from the 70-100ns simulations. The interaction analysis revealed that fortunellin was stabilized by the non-polar interactions with Leu162, Pro248, Ala249, Tyr264, Tyr264, Cys270, and Pro299 amino acids of the Plpro, and polar interactions including Gln250, Thr265, Asn267, Gln269, and His272. Notably, interaction with His272, one of the catalytic triad residues, suggests its inhibitory role (figure 2 (II-F)).

Furthermore, using MMGBSA analysis, the total binding energy ( $\Delta G_{\text{bind}}$  value), predominantly contributed by gas-phase interaction energy ( $\Delta G_{\text{gas}}$ ) and Vander Waal interaction energy ( $\Delta G_{\text{VDWAALS}}$ ), was calculated to be -29.6076kcal/mol with a standard deviation of  $\pm 4.3975$ kcal/mol (figure 2 (II-G) and table 1). Residue decomposition analyses revealed that the Tyr264 and Tyr268 residues majorly contributed with energy -3.41182 and -2.82612 kcal/mol respectively. Other residues including Glu161, Leu162, Asp164, Pro248, Asn267, Gln269, Cys270 and Gly271 were also involved in the contribution to the total binding energy favoring the PLpro-fortunellin complex formation (figure 2 (II-H)).

### **MD simulation and MMGBSA analysis of fortunellin-RdRp complex**

In the fortunellin-RdRp complex, the stability of the complex was validated by evaluating the RMSD and Rg value. RMSD was plotted for the 100ns time scale (figure 2 (III-A)). The equilibrium state and stable RMSD indicate the placement of ligand in the cavity of the receptor. A stable Rg value of 3.27 nm with no abrupt fluctuations indicates tight packing of the ligand-target complex (figure 2 (III-B)). The minimum distance between the fortunellin-RdRp fluctuated in between a short range of 0.16 to 0.22 nm indicating the close contact between them during the 100ns MD trajectory (figure 2 (III-C)). The residual mobility in the presence of fortunellin was determined by the RMSF analysis (figure 2 (III-D)). It is evident from the RMSF graph that the catalytic residues <sup>759</sup>SDD<sup>761</sup> and the divalent-cation-binding residue D618 for RdRp are among the most stable residues with minimized fluctuations, leading to a stable configuration of the complex. The formation of an average of three

H-bonds throughout simulation explains its affinity for RdRp (figure 2 (III-E)). In addition, to analyze the RdRp-fortunellin interactions, we used the representative snapshot of the most populated cluster obtained from the 70-100ns simulations. The interaction analysis revealed the polar interactions involving uncharged His439, His810 and Ser814; positively charged Lys545, Lys551, Arg555, Lys798, and Arg836, and negatively charged Asp618, Asp761, and Glu811 residues, respectively. Phe440, Phe 442, Tyr546, Ala547, Ile548, Ala550, Ala554, Trp617, Cys799, and Trp800 residues stabilize the complex via hydrophobic interactions. Also, extra stability is provided by the formation of H-bond with the backbone of Ala550, as well as Ile548 and Arg555. Ala550 behaves as a hydrogen bond doner whereas Ile548 and Arg555 act as H-bond acceptors (figure 2 (III-F)).

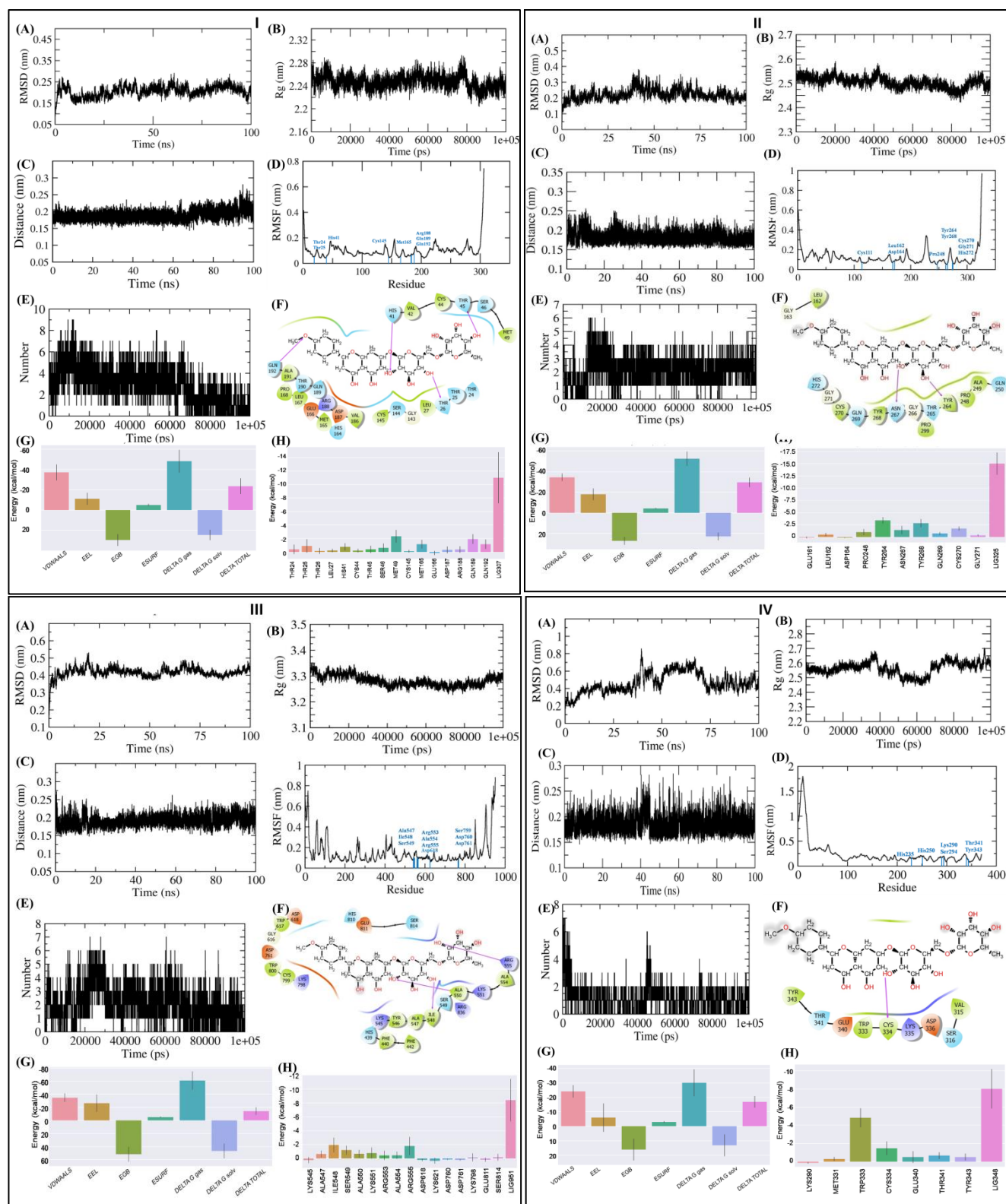
Furthermore, the stability of the RdRp-fortunellin was estimated using MMGBSA calculations. The binding free energy calculations using the MMGBSA revealed that the binding of fortunellin at the active site of protein is predominantly stabilized by gas-phase interaction energy ( $\Delta G_{\text{gas}}$ ) and Vander Waal interaction energy ( $\Delta G_{\text{VDWAALS}}$ ). The negative free binding energy of -14.2483kcal/mol with a standard deviation of  $\pm 5.6359$  kcal/mol, indicated the favorable binding (figure 2 (III-G)). The residues Lys545, Ala547, Ile548, Ser549, Ala550, Lys551, Arg553, Ala554, Arg555, Lys798, and Glu814 contributed towards the favorable energy indicating the involvement of these residues in fortunellin-RdRp complex stabilization (figure 2 (III-H)). Thus, targeting the RdRp active sites with fortunellin could be a potential therapeutic option for inhibition of coronavirus RdRp and thus viral replication.

### **MD and MMGBSA analysis of fortunellin-Endoribonuclease (NendoU) complex**

In fortunellin-endoribonuclease- complex, initially the RMSD value remained to be 0.4 nm for about 36 ns after which a sudden increase in RMSD up to 0.8nm was observed, such observations might be due to opening and closing of the active site that gives sufficient space to the ligand molecule to achieve new orientations. Around 75ns the complex regained conformational integrity with

fluctuating RMSD between 0.4 to 0.6 nm. Endoribonuclease-fortunellin complex was stabilized during 50-75ns (figure 2 (IV-A)). The average Rg value of 2.5 to 2.7 nm indicates the compactness of the formed complex (figure 2 (IV-B)). Fortunellin at a minimum distance of 0.24 nm with endoribonuclease suggests its proximity (figure 2 (IV-C)). To provide more detailed information of motions in NendoU upon binding fortunellin, RMSF as function of the residue number for the 100 ns trajectories were plotted. A stable RMSF profile of binding site residues His225, His250, Lys290, Ser294, Thr341, and Tyr343 suggests the thermodynamic stability of the endoribonuclease-fortunellin complex (figure 2 (IV-D)). Also, an average of three H-bonds was formed between target-ligand throughout the 100ns run, providing molecular recognition, stability, and overall conformation to the complex (figure 2 (IV-E)). In addition, to analyze the endoribonuclease-fortunellin interactions, we used the representative snapshot of the most populated cluster obtained from the 70-100ns simulations. Fortunellin was found to occupy the binding pocket of the endoribonuclease enzyme utilizing the polar amino acids Ser316 and Thr341; hydrophobic Val315, Trp333, Cys334, and Tyr343,; and charged Lys335Asp336 and Glu340 amino acids respectively. It was also found to form H-bond with Cys334 that additionally contributes to the intactness of the molecule in its position (figure 2 (IV-F)).

Furthermore, the binding free energy calculations using the MMGBSA revealed that the binding of fortunellin at the active site of protein is predominantly stabilized by gas-phase interaction energy ( $\Delta G_{\text{gas}}$ ) and Vander Waal interaction energy ( $\Delta G_{\text{VDWAALS}}$ ). The overall binding energy was found to be -16.8392kcal/mol with a standard deviation of  $\pm 3.8733$  kcal/mol as indicated by figure 2 (IV-G). The negative binding energy was contributed by seven residues. The Trp333 contributed majorly to the stability of the ligand with energy equal to -4.83118kcal/mol, and the residues Lys290, Thr341, and Tyr343 lining the catalytic pocket of the enzyme also contributed to overall affinity. In addition, the energy contributions of Met331, Cys334, and Glu340 may favor the fortunellin-endoribonuclease complex formation (figure 2 (IV-H)).



## **MD simulation and MMGBSA analysis of fortunellin-replicase (monomer) complex at NSP-8 and dimer interface binding site**

We observed that fortunellin binds to two sites that are both critical in viral replication: the NSP-8 binding site and the dimeric interface of the replicase enzyme. The NSP-8 binding site of replicase bound with fortunellin was first explored using the MD simulations. Throughout the 100ns timescale, the complex maintained a steady RMSD value of 0.59nm (figure 3 (I-A)). The rigidity and compactness of the complex were also evaluated by the equilibrated value of Rg at 1.5nm (figure 3 (I-B)). The distance between the ligand and receptor was maintained at 0.2 nm (figure 3 (I-C)). The RMSF values of all the interacting residues including Leu43, Cys74, Arg75, Phe76, Lys87, Leu89, Phe91, Leu104, Ala108, Val111, and Leu113, were found to be ~0.1nm (figure 3 (I-D)). The ligand-receptor on average consists of at least 2-3 H-bonding contributing to intact position of ligand in the receptor pocket (figure 3 (I-E)). In addition, to analyze the fortunellin-replicase interactions at the NSP-8 binding site, we used the representative snapshot of the most populated cluster obtained from the 70-100ns simulations. We observed that fortunellin occupies the binding site residues Leu46, Lys87, Val111, and Leu113, required for NSP-8 attachment thus, making the site occupied and may prevent its binding. The complex formed is stabilized by several hydrophobic, hydrophilic, and charged interactions with Leu10, Tyr32, Leu46, Phe76, Val77, Val86, Leu89, Val103, Leu107, Val111, and Leu113; Gln12, Thr78, Ser106, and Thr110; Arg11, Lys85 and Lys87 respectively. Also, the formation of one H-bonds with the backbone of Leu10 provides extra stability to the complex formation (figure 3 (I-F)).

The binding energy of -29.9465kcal/mol with a standard deviation of  $\pm 5.6596$ kcal/mol binding, predominantly contributed by gas-phase interaction energy ( $\Delta G_{\text{gas}}$ ) and Vander Waal interaction energy ( $\Delta G_{\text{VDWAALS}}$ ) (figure 3 (I-G)) reveals favorable ligand-receptor interactions. Furthermore, MMGBSA analysis revealed that Gln12, Leu30, Tyr32, Leu46, Phe76, Thr78, Lys87, Leu107, Thr110, Val111 and Leu113 are the residues contributing to the binding energy (figure 3 (I-H)).

Next, we explored the fortunellin binding at the dimeric interface of the replicase enzyme. Dimerization of the corona viral Nsp9 proteins is known to be required for its function and thus, occupying the dimer forming surface prevents the protein to become functionally active. The RMSD was found to be fluctuating in a narrow range of 0.25 to 0.33nm (figure 3 (II-A)). The complex formed was highly compact and rigid (figure 3 (II-B)). This was evident from a stabilized value of Rg at 1.42nm. Also, the minimum distance between ligand and receptor was maintained at 0.2 nm (figure 3 (II-C)). The RMSF of the GXXXG domain responsible for dimer formation was observed to be stabilized upon ligand binding at 0.09nm (figure 3 (II-D)). The complex had an average of 2 H-bonds throughout. After 80ns simulations, the number of H-bonds increased from 2 to 7 (from the initial value) (figure 3 (II-E)). Additionally, to analyze the Replicase-fortunellin interactions at dimeric interface, we used the representative snapshot of the most populated cluster obtained from the 70-100ns simulations. Interaction analysis revealed that fortunellin was stabilized at dimeric interface contributed by GxxxG domain residues Gly101, Met102, Leu104, and Gly105. It also interacts with polar residues Gln114; and non-polar residues Phe76, Met102, Leu104 Leu107, Ala108, Ala109, Val111, and Leu113. The charged amino acids Asp79 and Arg112 contribute in binding the ligand. Also, fortunellin showed five hydrogen bond interactions with residues Asp79 (two H-bonds), Val111, Arg112 and Leu113 (figure 3 (II-F)).

MMGBSA study estimated the overall binding free energy to be -23.2796kcal/mol, with a standard deviation of 7.4088kcal/mol (figure 3 (II-G)). The binding of fortunellin was mainly contributed by gas-phase interaction energy ( $\Delta G_{\text{gas}}$ ) and Vander Waal interaction energy ( $\Delta G_{\text{VDWAALS}}$ ). The residues Ser6, Pro7, Ser106, Ala108, and Ala109, in addition to the GxxxG domain residues, contributed to the observed binding energy (figure 3 (II-H)). All of this suggests proper complex formation folding and stabilization with less dynamic mobility of the receptor and less conformational alterations to the overall enzyme structure. Thus, occupying the enzyme's interface may prevent dimerization and thus activation, affecting its functions. Thus, Fortunellin may potentially inhibit the NSP-8 activity by targeting the replicase enzyme.



## MD simulation and MMGBSA analysis of fortunellin-replicase (dimer) complex

We also investigated the binding and stability of fortunellin at the binding pocket formed by replicase dimerization. Replicase activation takes place by dimer formation that further binds to RNA and NSP-8 to participate in replicase activity [57]. The consistent RMSD value of  $0.28 \pm 0.04$  nm with lower deviation indicated its interaction stability (figure 3 (III-A)). A compact structure was formed with an almost stable Rg value of 2.0 nm (figure 3 (III-B)). The minimum distance between the ligand and receptor complex was also determined for the entire 100ns simulation run and was found to be stable at 0.19nm throughout (figure 3 (III-C)). The residues lining the cavity including G101, MET102, Val103, Leu104, Gly105 and Leu16 showed stabilized RMSF (figure 3(III-D)). The stability of the complex was also checked by the formation of the number of H-bonds between the ligand and the receptor. Fortunellin was stabilized in the cavity with an average of five H-bonds throughout the simulation time (figure 3 (III-E)). We have also analyzed the representative snapshot of the most populated cluster obtained from the 70-100ns simulations for molecular interactions. Fortunellin is stabilized mainly with the help of polar and non-polar interactions of Chain A: Met1, Asn2, Leu5, Ser6, Pro7, Val8, Leu98 and Met102; and Chain B: Pro72, Pro73, Cys74, Arg75, Phe76, Val77, Thr78, Asp79, Lys87, Phe91, Leu104, Gly105, Leu107, Ala108, Thr110, and Val111 residues. These interactions altogether may potentially stabilize the ligand within the pocket of the receptor (figure 3 (III-F)).

MMGBSA analysis yielded an overall binding free energy of -45.9116kcal/mol with a standard deviation of  $\pm 4.8148$ kcal/mol (figure 3 (III-G)). The binding of fortunellin was mainly contributed by gas-phase interaction energy ( $\Delta G_{\text{gas}}$ ) and Vander Waal interaction energy ( $\Delta G_{\text{VDWAALS}}$ ). This binding energy highly favours the binding of fortunellin to the dimeric form of replicase enzyme. As shown in figure 3 (III-H), residues of both the chains contribute to this energy including Met1, Leu5, Ser6, Pro7, Val8, and Leu98 residues of Chain A and Glu71, Pro72, Cys74, Arg75, Phe76, Val77, Leu89, Phe91, Leu104, Leu107 and Val111 residues of Chain B respectively. Thus, fortunellin

binding to the cavity at dimeric contact point of replicase may prevent it from binding with RNA and NSP-8 essential for viral propagation.

### **MD simulation and MMGBSA analysis of fortunellin-helicase complex**

The structural change of fortunellin in complex with SARS-CoV-2 Helicase was estimated using root-mean-square deviation (RMSD). The complex was observed with an average RMSD value of 0.35 nm (figure 3 (IV-A)). The value of Rg was observed to be stabilized at  $2.85 \pm 0.03$  nm (figure 3 (IV-B)). The minimum distance between fortunellin and Helicase was stabilized within 8 ns at 0.18 nm and was maintained till the simulation end (figure 3 (IV-C)). The RMSF value per residue, in the MD simulation of the complex was plotted. Major grooves in the plot were occupied by the catalytic site residues including Lys288, Ser289, Asp374, Glu375, and Arg567. Low fluctuations of these residues upon ligand binding indicated its stability as a complex (figure 3 (IV-D)). The analysis of the number of hydrogen bond suggests that fortunellin not only fits well into the catalytic pocket of Helicase, but also make appropriate hydrogen bonds necessary for proper stability within the protein. An average of four H-bonds was found to be formed between fortunellin and Helicase enzyme throughout the simulation (figure 3 (IV-E)). Additionally, to analyze the Helicase-fortunellin interactions, we used the representative snapshot of the most populated cluster obtained from the 70-100ns simulations. The structure is stabilized via polar Thr286, Ser289, His290, Ser310, and Ser539 interactions, hydrophobic Ala312, Ala313, Ala316, Leu317, and Cys444 interactions, charged Lys288, Lys320, Asp374, Glu375, Arg442, Arg443, and Glu540 interactions along with two H-bonded interactions each with Ser289 and Lys320 residues. The interaction with catalytically and functionally important residues Lys288, His290, and Arg443 enables their masking and thus, making them unavailable for their role in viral replication machinery, ultimately inhibiting the protein functions (figure 3 (IV-F)). Using MMGBSA, the overall binding free energy was observed to be -21.0360 kcal/mol with a standard deviation  $\pm 4.4760$  kcal/mol as shown in figure 3 (IV-G). The residues contributing to this negative energy include the catalytically important residues His290,

Arg442 and Arg443. Along with it 14 more residues that are Pro283, Gly285, Thr286, Gly287, Ser289, Ala312, Ala313, Ala316, Leu317, Asp374, Glu375, Gly538, Ser539 and Glu540 also played role in interaction of fortunellin to helicase pocket (figure 3 (IV-H)).

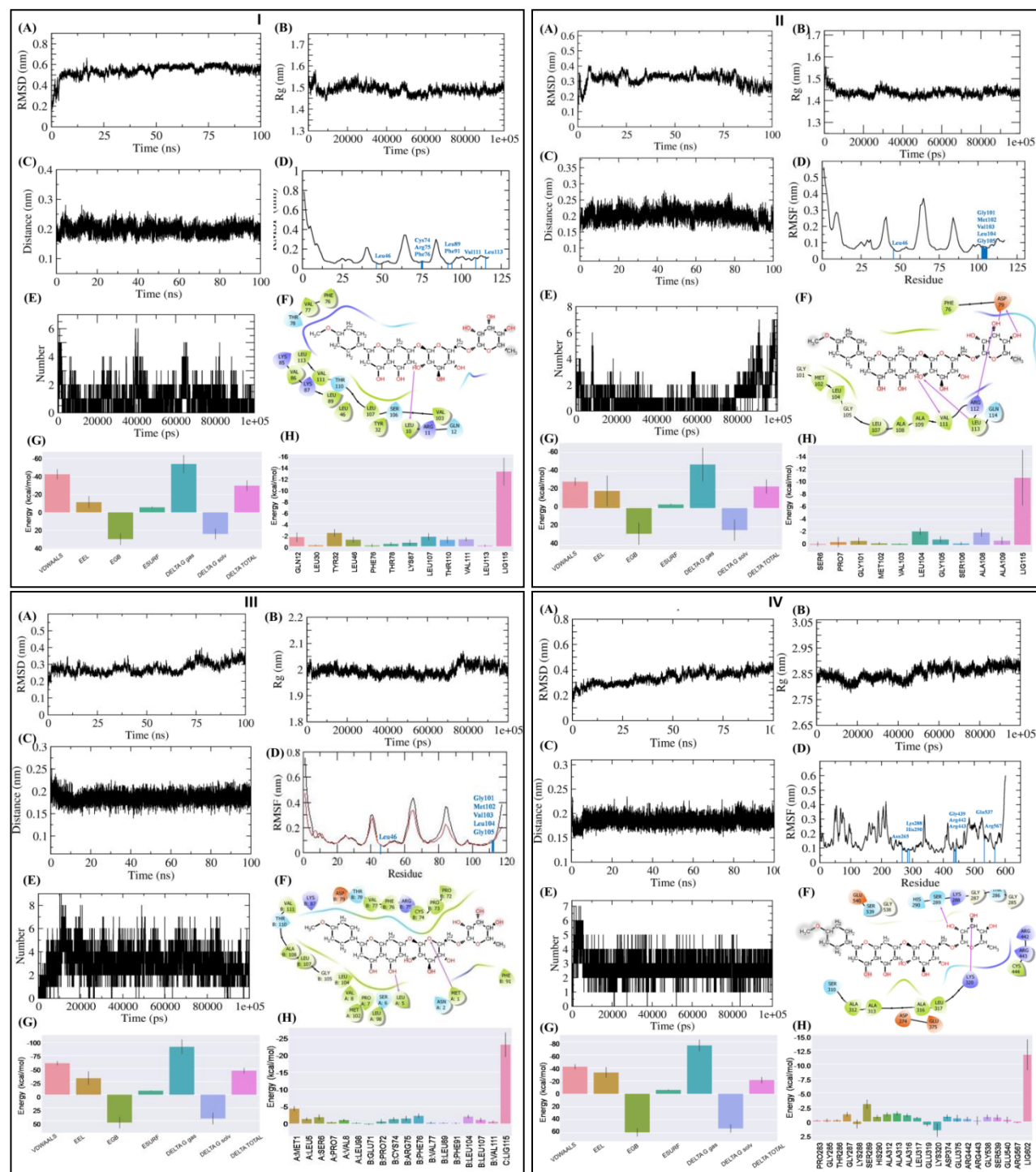


**figure 3. MD analysis of fortunellin-SARS-CoV-2 complex. I) Replicase (monomer), II) Replicase (monomer) at NSP8 site III) Replicase (dimer), and IV) Helicase. The plots are: (A) RMSD, (B) RMSF, (C) Rg, (D) number of H-bonds, (E) minimum distance, (F) distribution of H-bonds, (G) overall binding energy from different energy components through MM-GBSA calculations(H) residue wise contribution to the binding energy of the complex.**

## **MD simulation and MMGBSA analysis of Fortunellin-2'O Methyltransferase complex**

The SARS-COV-2 2'-O-methyltransferase (MT)) complexed with fortunellin was evaluated for its ability to decrease the dynamicity of the enzyme. Since this enzyme is most active in a flexible form; the flexibility was minimized by binding it to a ligand molecule. The RMSD value of  $0.36 \pm 0.03$  nm was found to be stable throughout the simulation (figure 4 (I-A)). The residual fluctuations were observed to be very low, indicating less flexibility of the complex. The binding of the ligand leads to proper folding of the protein that was evident from the low fluctuating value of Rg. Also, an average Rg value of  $1.91 \pm 0.03$  nm reveals that the compactness of the formed complex was achieved (figure 4 (I-B)). The minimum distance between the receptor and the complex was maintained at 0.22 nm throughout (figure 4 (I-C)), indicating that the ligand was in close proximity of the receptor throughout the time period of 100 ns. A stable RMSF value of Leu16, Cys74, Arg75, Phe76, Leu89, Phe91, Val111, and Leu113 suggest the stabilized inhibitor binding site in presence of fortunellin (figure 4 (I-D)). The formation of two H-bonds on average adds to the stability of the ligand-target complex (figure 4 (I-E)). The H-bonds were observed to increase to five interactions within 90-100. In addition, to analyze the fortunellin-MT interactions, we used the representative snapshot of the most populated cluster obtained from the 70-100ns simulations. MT-Fortunellin complex was stabilized mainly via hydrophobic interactions with Cys6913, Ala6914, Pro6932, Phe6947, Tyr6950, Cys6952, Leu7093, and Val7094. Polar interactions occur with Thr6915, Thr6934, Thr6949, Gln6956, Gln6957, Asn7095 and Asn7096. Charged interactions take place with Lys6933 and Lys6935. Residues Val7094, Asn7095, Asn7096 contributed three H-bonds to stabilize the fortunellin-MT complex. During MD simulation, the fortunellin accommodates to an adjacent cavity close to the RNA methylation site. However, its bulkier size and stable binding may still potentially hinder the incoming RNA and the methylation process (figure 4 (I-F)). The overall binding energy favored complex formation and was observed to be -24.3314 kcal/mol with a standard deviation of  $\pm 7.4392$  kcal/mol (figure 4 (I-G)). The energy was mainly contributed by the residues Ala6914, Thr6915, Asp6931, Pro6932, and Phe6947 as shown in figure 4 (I-H).

## MD simulation and MMGBSA analysis of Fortunellin-Spike (S-RBD) complex

SARS-CoV-2 spike receptor-binding domain binds with the host ACE2 receptor leading to the viral entry in the host cell [58, 59]. Targeting this protein is a clear and direct approach to inhibit the COVID-19 infection. Fortunellin bound to spike protein was obtained from the docking studies. The docking studies yielded Fortunellin bound to spike protein. RMSD analysis revealed that the complex reaches conformational stability at 8.5 ns with an RMSD of 0.8 nm and remains in this conformation for the remainder of the simulation session (figure 4 (II-A)). Furthermore, the equilibrated value of Rg at 2.1 nm shows the rigidity and compactness of the complex (figure 4 (II-B)). A minimum distance of 0.2 nm between the ligand and receptor was maintained throughout the simulation indicates that ligand is occupied in the pocket of the receptor (figure 4 (II-C)). The residues in the pocket-forming the active site for binding of ligand had a low RMSF between 0.1-0.22 nm; this could be attributed to the low b-factor in that region owing to its structural confirmation (figure 4 (II-D)). Although there was an observed decrease in the number of H-bonds after 40 ns, an average of 3-4 H-bonds existed throughout the simulation (figure 4 (II-E)). In addition, to analyze the Spike-fortunellin interactions, we used the representative snapshot of the most populated cluster obtained from the 70-100ns simulations. Fortunellin showed interaction with critical residues of RBD including Leu455, and Gln493, of SARS-CoV2. In addition, it forms hydrophobic, polar and charged interactions with Leu455, Phe456, Tyr473, Ala475, Cys488, Tyr489, Phe490, Pro491 and Leu492; and Gln493; Arg457, Lys458, and Glu484 respectively.(figure 4 (II-F)). Glu484, Phe490 (two H-bonds), and Gln493 all contributed to four H-bonds. These interactions, when combined, stabilized the Fortunellin-spike complex. As per the MM-GBSA energy estimates, the complex produced is stable, with a binding energy of -23.3499kcal/mol and a standard deviation of  $\pm 6.61018$ kcal/mol (figure 4 (II-G)). Fortunellin binding was influenced mostly by gas-phase interaction energy ( $G_{\text{gas}}$ ) and Vander Waal interaction energy ( $G_{\text{VDWAALS}}$ ). As shown by figure 4 (II-H), the most energetic residues are Tyr449, Leu455, and Gln493, with binding energies of -0.1636, -1.12414, and -1.6523kcal/mol, respectively.

## MD simulation and MMGBSA analysis of fortunellin-nucleocapsid (N-NTD) complex

The atomistic dynamics movements and conformational variations of fortunellin-Nucleocapsid (NTD) complex C $\alpha$  backbone atoms revealed initial fluctuations in RMSD values up to 60 ns and thereafter remained steady at  $0.62 \pm 0.04$  nm until the molecular simulation of 100ns (figure 4 (III-A)). This variation in RMSD is indicative of fortunellin conformational changes in the receptor pocket to acquire the optimal stable connections. The structure's compactness was maintained and achieved at 60ns, as shown in figure 4 (III-B), where the Rg value stabilised at 1.5 nm after this time scale. Furthermore, the complex's stability was assessed by the minimal distance between the ligand and receptor during complex formation, as shown in figure 4 (III-C), and was found to be stable in the range of 0.16 to 0.22 nm. The key substrate binding residues (with 5Å zone) were Arg89, Ala91, Thr92, Arg93, Tyr110, Arg150, Asn151, and Pro152, which had a low RMSF value of 0.22-0.25nm (figure 4 (III-D)). Figure 4 (III-E) shows that an average of four H-bonds were observed to maintain throughout the simulation. Furthermore, we used the representative snapshot of the most populated cluster generated from the 70-100ns simulations to analyze the N-NTD-fortunellin interactions. Fortunellin was found to stabilize through non-polar interactions with Pro43, Leu46, Pro47, Ala51, Ala91, Ile95, Leu105, Tyr110, and Tyr112 amino acid residues; polar interactions with Gln44, Asn48, Asn49, and Thr92; and charged interactions with Arg89, Arg93, Arg94, Asp99, and Lys101 amino acid residues of the main chain. Gly45 and Arg94 both contributed to the H-bond. These connections are strong enough to keep the complex's structure intact, hence reducing viral RNA interaction and infectivity to the host (figure 4 (III-F)). Energy calculations using MM-GBSA revealed effective binding energy of -28.4610kcal/mol with a standard deviation of  $\pm 7.7635$ kcal/mol, indicating the formation of a favorable complex (figure 4 (III-G)). The residues Asn48, Asn49, Ala91, Arg93, and Tyr110, Ala51, Arg89, Thr92, Arg108, Tyr112, Pro118, Arg150, Pro152, and Glu175 all contributed to the complex's binding energy and stability (figure 4 (III-H)). All of these interactions help to keep the N-NTD and fortunellin complex stable.

## **MD simulation and MMGBSA analysis of fortunellin-nucleocapsid (N-CTD) complex**

Similarly, the stability of the Nucleocapsid CTD complexed with fortunellin was examined. The RMSD value was observed to vary between  $0.70 \pm 0.12$  nm (figure 4 (IV-A)). The low fluctuations indicate that the protease has not undergone significant structural changes. The Rg value varied within a narrow range of  $1.7 \pm 0.1$  nm, suggesting the compactness and integrity of the produced complex (figure 4 (IV-B)). The distance between fortunellin and nucleocapsid CTD was found to a minimum of 0.2 nm (figure 4 (IV-C)). The important residues had a low RMSF value of 0.25 nm on average throughout the simulation (figure 4 (IV-D)). Throughout the simulation, there are an average of 2-3 H-bonds, showing the protein-ligand complex's stability (figure 4 (IV-E)). Furthermore, we used the representative snapshot of the most populated cluster acquired from the 70-100ns simulations to analyze the CTD-fortunellin interactions. Fortunellin showed non-polar hydrophobic interactions with Phe274, Phe286, Ile304, Ala305, Phe307, Ala308, Pro309, Ala311, Phe314, Phe315, Trp330, Leu331, Tyr333, Ala336, Ile337, Leu353, and Ile357 residues in complex with nucleocapsid C-terminal dimerization domain. During complex formation, there were polar contacts with Gln260, Gln281, Thr282, Gln283, Asn285, Ser310, Ser312, Ser318, Thr325, and Thr332 residues, as well as a charged interaction with Arg277 and Glu280 (figure 4 (IV-F)). MM-GBSA energy calculations revealed that fortunellin has the highest binding affinity to N-CTD of any target under consideration. Figure 4 (IV-G) depicts the overall binding energy as -51.3094kcal/mol with a standard deviation of  $\pm 3.7282$ kcal/mol. Arg259, Gln260, Phe274, Arg277, Gly284, Asn285, Phe286, Leu291, Trp301, Ile304, Phe307, Ala308, Pro309, Ser310, Ala311, Phe314, Phe315, Tyr333, Ile337, Leu353, and Ile357 are among the residues that contribute to binding affinity (figure 4 (IV-H)).

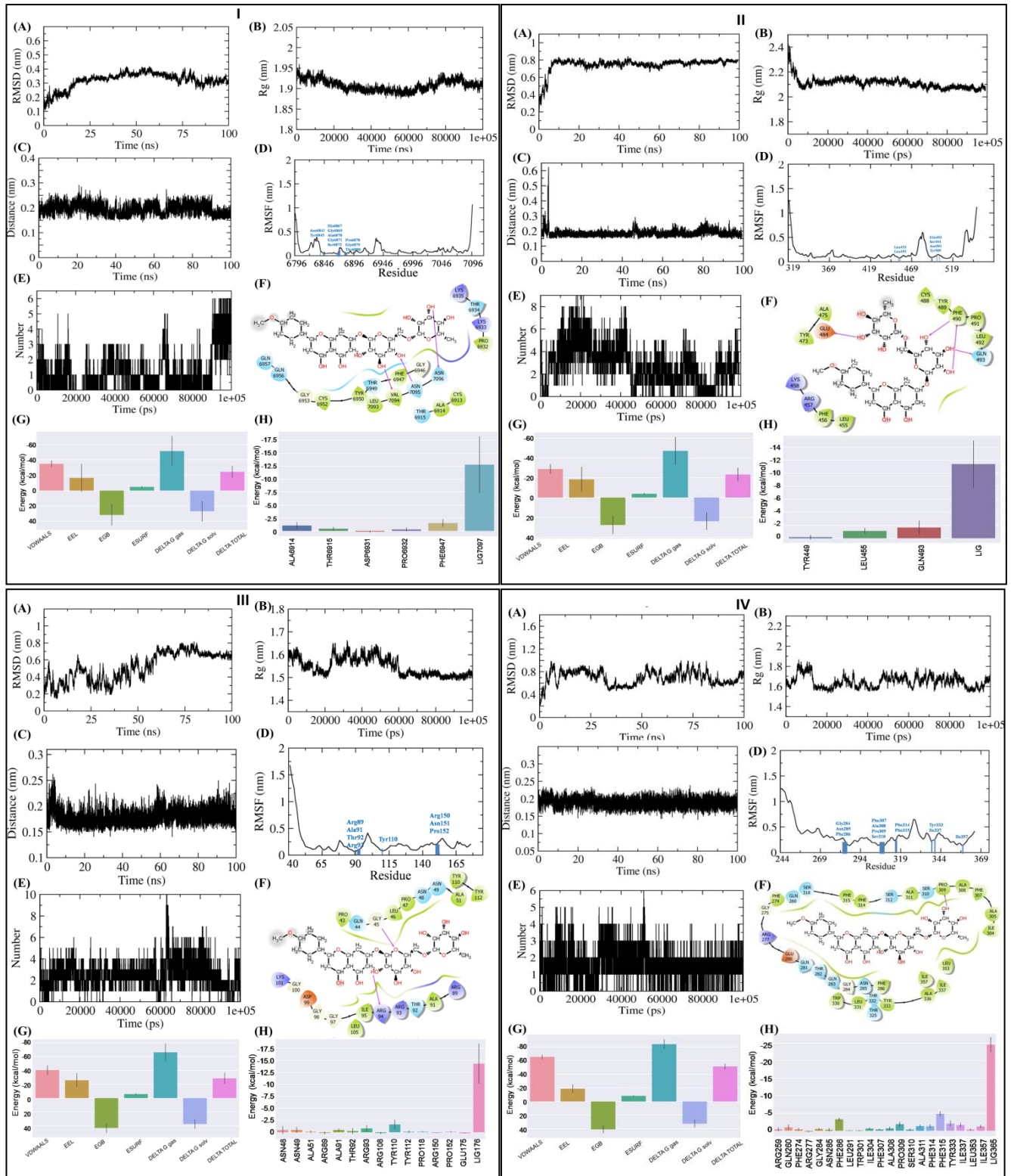


**Figure 4.** MD analysis of fortunellin-SARS-CoV-2 complex. I) 2'O Methyltransferase, II) Spike-RBD III) Nucleocapsid (N-NTD) and IV) Nucleocapsid (C-NTD). The plots are: (A) RMSD, (B) Rg, (C) Minimum distance between fortunellin and SARS-CoV-2 target (D) RMSF (E) Number of H-bonds (F) Interaction between fortunellin and SARS-CoV-2 target (G) Binding energy from different energy components through MM-GBSA calculations (H) Residue wise contribution to the binding energy of the complex.



**Table 1.** Binding free energy components of major protein targets of SARS CoV-2 with fortunellin calculated by MM-GBSA analysis.

SARS CoV-2 Targets	$\Delta E_{VDW}$	$\Delta E_{EEL}$	$\Delta G_{GB}$	$\Delta G_{SURF}$	$\Delta G_{gas}$	$\Delta G_{Sol}$	$\Delta G_{bind}$
<b>Main protease</b>	-37.0752	-11.0390	29.6084	-4.9820	-48.1142	24.6263	<b>-23.4878</b>
(Mpro)	$\pm 7.6638$	$\pm 5.7167$	$\pm 5.6156$	$\pm 0.9982$	$\pm 10.9903$	$\pm 4.9268$	$\pm 7.5613$
<b>Papain like protease</b>	-34.4708	-18.0303	27.1233	-4.2298 $\pm$	-52.5011	22.8935	<b>-29.6076</b>
(PLpro)	$\pm 3.5312$	$\pm 5.5609$	$\pm 3.7101$	0.3646	$\pm 6.7571$	$\pm 3.5621$	$\pm 4.3975$
<b>RNA dependent RNA polymerase (RdRp)</b>	-34.7177	-26.3288	51.8063	-5.0080 $\pm$	-61.0466	46.7983	<b>-14.2483</b>
	$\pm 6.4125$	$\pm 13.0760$	$\pm 11.2326$	0.8122	$\pm 13.7200$	$\pm 10.9732$	$\pm 5.6359$
<b>Endo-ribo nuclease</b>	-24.0951	-5.9482 $\pm$	16.1503	-2.9462	-30.0433	13.2042	<b>-16.8392</b>
(NendoU)	$\pm 4.1713$	9.6601	$\pm 7.3866$	$\pm 0.4949$	$\pm 9.1564$	$\pm 7.4130$	$\pm 3.8733$
<b>Replicase (monomer)-NSP-8 binding site</b>	-42.6222	-11.4360	29.8224	-5.7107 $\pm$	-54.0582	24.1117	<b>-29.9465</b>
	$\pm 5.5207$	$\pm 6.5480$	$\pm 6.2807$	0.7606	$\pm 9.7724$	$\pm 5.8585$	$\pm 5.6596$
<b>Replicase (monomer) dimer interface</b>	-28.4924	-18.5108	27.6375	-3.9139	-47.0032	23.7236	<b>-23.2796</b>
	$\pm 4.2468$	$\pm 16.4878$	$\pm 11.8362$	$\pm 0.6781$	$\pm 17.9508$	$\pm 11.3323$	$\pm 7.4088$
<b>Replicase (dimer)</b>	-60.0795	-31.4229	53.1305	-7.5398	-91.5024	45.5908	<b>-45.9116</b>
	$\pm 3.8148$	$\pm 12.7593$	$\pm 10.9148$	$\pm 0.3898$	$\pm 13.8058$	$\pm 10.7129$	$\pm 4.8148$
<b>Helicase</b>	-41.6268	-32.8214 $\pm$	59.3551	-5.9430	-74.4482	53.4121	<b>-21.0360</b>
	$\pm 3.5150$	7.9387	$\pm 6.1387$	$\pm 0.3940$	$\pm 8.5248$	$\pm 5.9690$	$\pm 4.4760$
<b>2'-O-methyltransferase</b>	-34.8640	-16.4995	31.7177	-4.6856	-51.3635	27.0321	<b>-24.3314</b>
	$\pm 4.1705$	$\pm 17.8013$	$\pm 13.5921$	$\pm 0.7716$	$\pm 19.4495$	$\pm 13.0094$	$\pm 7.4392$
<b>Spike receptor binding domain (S-RBD)</b>	-28.7552	-18.4254	27.6757	-3.8449 $\pm$	-47.1806	23.8308	<b>-23.3499</b>
	$\pm 4.6937$	$\pm 12.3420$	$\pm 8.9006$	0.6426	$\pm 13.7162$	$\pm 8.5381$	$\pm 6.6018$
<b>Nucleocapsid N-terminal RNA binding domain (N-NTD)</b>	-40.3240	-25.6714	43.3076	-5.7732	-65.9954	37.5344	<b>-28.4610</b>
	$\pm 6.5644$	$\pm 9.8105$	$\pm 6.8286$	$\pm 0.8931$	$\pm 12.3146$	$\pm 6.4711$	$\pm 7.7635$
<b>Nucleocapsid C-terminal dimerization domain (N-CTD)</b>	-65.3242	-18.5982	40.8292	-8.2162 $\pm$	-83.9224	32.6130	<b>-51.3094</b>
	$\pm 3.1529$	$\pm 5.9898$	$\pm 5.5015$	0.4305	$\pm 7.0581$	$\pm 5.3824$	$\pm 3.7282$

All energies are in kcal/mol along with their standard deviation.  $\Delta E_{VDW}$ , van der Waals contribution from MM;  $\Delta E_{EEL}$ , electrostatic energy as calculated by the MM force field;  $\Delta G_{GB}$ , the electrostatic contribution to the solvation free energy calculated by GB;  $\Delta G_{SURF}$ , solvent-accessible surface area;  $\Delta G_{Sol}$ , solvation free energy;  $\Delta G_{gas}$ , gas-phase interaction energy and  $\Delta G_{bind}$ , is the binding free energy.

## Molecular and ADMET properties of Fortunellin

The various molecular and physicochemical properties of fortunellin were calculated and the observed results are listed in Supplementary table S3. The molecular weight of Fortunellin is 592.180 Da with 14 H-bond acceptors and 7 H-bond donors. The number of rotatable bonds was found to be seven, thus, provide enough flexibility to the compound to rotate about its axis as well as interact with the receptor residues. It constitutes five rings with 10 atoms in the biggest ring. There exists no formal charge. The log of aqueous solubility (logS) of Fortunellin is -3.891 mol/L and the log of octanol/water partition coefficient (logP) is 0.568, indicating its nature to be more hydrophilic than hydrophobic. Also, the value of logP at physiological pH was found to be in an optimum range. After satisfactory results from the molecular features, fortunellin was further evaluated for its ADMET properties. We calculated the pharmacokinetic properties of Fortunellin using pkCSM and Admetlab 2.0 tools (Supplementary table S4). We observed a preferable water solubility of -2.837 log mol/L, with reliable gastric absorption that complied with the stated bioavailability score. We found that Fortunellin was skin impermeable. It is also known as P-glycoprotein substrate, a cellular efflux pump that pumps out drugs to extracellular fluid and does not inhibit any P-glycoprotein [60]. An optimum volume distribution (VD<sub>ss</sub>) of 0.603 L/kg and 17.24% of unbound fraction of drug in the body was predicted. It showed a low probability of 0.293 for passing the blood-brain barrier (BBB), and thus would not cause any side effects to CNS. Moreover; the cytochrome P450 (CYP P450) enzymes family is not predicted to have any effects on encountering fortunellin in the body. The compound showed to have a probability of a short half life time and thus would be consumed quickly without interfering with other functionalities of the cell. Fortunellin does not provoke skin sensitization and was not predicted to have AMES, hERG I & II, minnow, respiratory, and hepatotoxicity. Overall, these data confirm that the fortunetelling is an example of a multitargeting compound affecting the Mpro, Plpro, RdRp, NendoU, replicase (monomer as well as dimer forms), Helicase, 2'O-methyltransferase, S-RBD, N-NTD, and N-CTD proteins that are necessary for viral replication, growth, invasion, and infectivity.

## Identification of targets of fortunellin in Covid-19 infected host cells/organoids

We identified 129 host proteins that could be targeted by fortunellin (Supplementary table S5) using Swiss Target Prediction (STP) [46] and the Similarity Ensemble Approach (SEA) [45]. We retrieved 500 up-regulated genes from SARS-CoV-2 infected human NHBE cells (GSE147507), lung cells (GSE147507), pancreatic organoids (GSE151803), colon organoids (GSE148696), liver organoids (GSE151803), and cornea organoids (GSE164073) using the Enrichr library "Covid-19 Related Gene Sets 2021." In NHBE cells, fortunellin targets 11 genes, 10 genes in lung cells, 6 genes in pancreatic organoids, 8 genes in colon organoids, 7 genes in liver organoids, and 8 genes in cornea organoids (figure 5, Supplementary table S6)

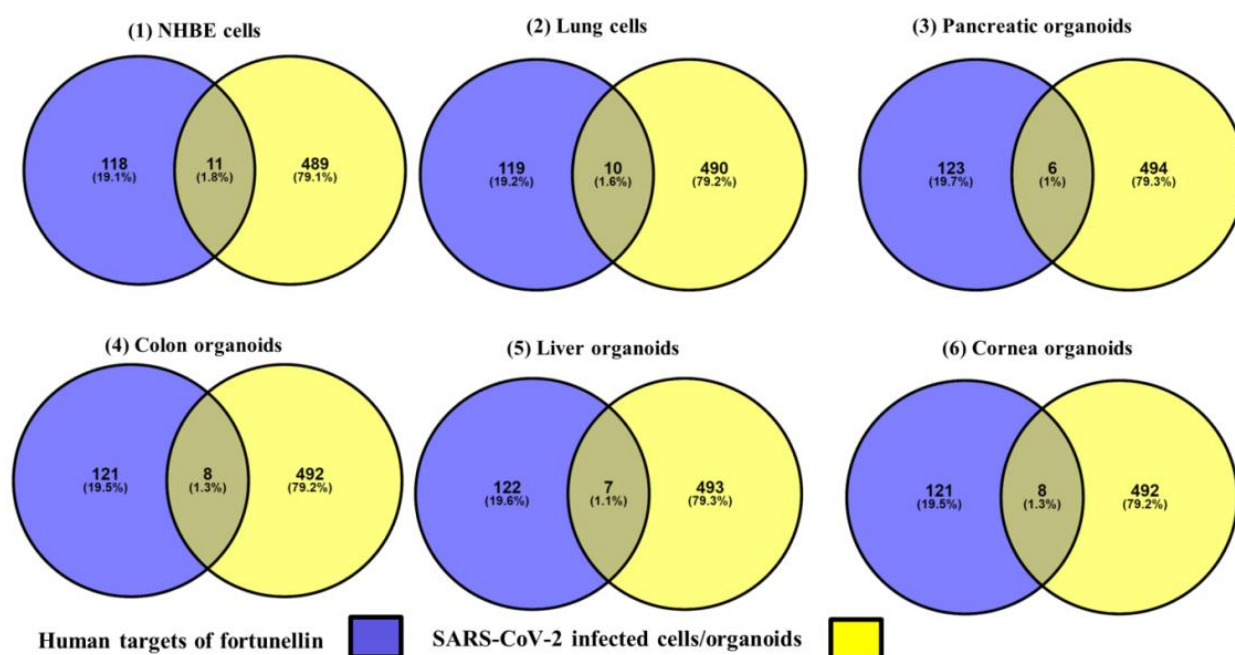


**Figure 5.** Venn diagram showing targets of fortunellin in Covid-19 infected cells/organoids

## Functional enrichment analysis of gene targets of fortunellin in NHBE cells

For the functional enrichment analysis, we identified the 11 gene targets of fortunellin in NHBE cells, including FN1, PTGS2, TNF, IGFBP3, EPHA2, LGALS9, AKR1B1, XDH, MMP1, VEGFA,

and IL6 utilizing biological processes (BP), molecular functions (MF), and cellular components (CC). Positive regulation of acute inflammatory responses, regulation of transforming growth factor-beta production, regulation of neuro-inflammatory responses, cytokine-mediated signalling pathway, positive regulation of leukocyte migration, regulation of the p38MAPK cascade, positive regulation of macromolecule metabolic process, and regulation of chemokine production were among the BPs identified (figure 6(1-A)). With statistically significant p-values, the fortunellin targets IL6, TNF, and VEGFA genes that were shown to be implicated in cytokine activity, receptor-ligand activity, growth factor activity, growth factor receptor binding, and cytokine receptor binding (figure 6(1-B)). Furthermore, its role in the endoplasmic reticulum lumen, platelet alpha granule lumen, and intracellular organelle lumen was revealed by cellular components analysis (figure 6 (1-C)).

#### **Functional enrichment analysis of gene targets of fortunellin in lung cells**

TNF, ADRA2A, CYP19A1, LGALS9, CD38, CA12, HCAR2, MMP8, CASP1, and CA1 were among the 10 gene targets of fortunellin in lung cells included in the functional enrichment study. As major biological processes, we identified negative regulation of lipid catabolic and metabolic processes, positive regulation of NIK/NF-kappaB signaling, positive regulation of interleukin-1 beta production, positive regulation of intracellular signal transduction, positive regulation of interleukin-6 production, and positive regulation of MAPK cascade (figure 6(2-A)). Cysteine-type endopeptidase activity, which is engaged in the apoptotic signalling pathway as well as in the execution phase of apoptosis, and tumor necrosis factor receptor binding were identified as molecular functions related to the genes targets CASP1 and TNF (figure 6(2-B)). Furthermore, it was found to be involved in three statistically significant cellular components, namely Collagen-containing extracellular matrix, tertiary granule lumen, and Specific granule lumen (figure 6(2-C)).

### **Functional enrichment analysis of gene targets of fortunellin in pancreatic organoids**

For the functional enrichment analysis, we used TNF, ADRA2C, ECE1, LGALS1, ABCB1, and CBS, which are all gene targets of fortunellin in pancreatic organoids. Positive regulation of signaling, regulation of peptide hormone secretion, positive regulation of intracellular signal transduction, regulation of insulin secretion, regulation of protein secretion, positive regulation of (IkappaB kinase/NF-kappaB signalling, regulation of programmed cell death, regulation of fever generation, positive regulation of anion transmembrane transport, and cellular response are just a few of the biological processes that it is involved in (figure 6(3-A)). The enriched molecular functions and cellular components were also investigated, and it was discovered that they were primarily involved in protein homo-dimerization activity, as well as the external side of the apical plasma membrane, clathrin-coated vesicle, and membrane raft (figures 6(3-B) and 6(3-C)).

### **Functional enrichment analysis of gene targets of fortunellin in colon organoids**

TNF, ADRA2C, ECE1, LGALS3, LGALS1, MMP7, MMP1, and ALDH1A2 were employed as fortunellin gene targets in colon organoids functional enrichment analysis. Positive regulation of dendritic cell differentiation, positive regulation of leukocyte differentiation, positive regulation of cellular component biogenesis, regulation of dendritic cell differentiation, positive regulation of cellular component organization, regulation of protein-containing complex assembly, positive regulation of protein-containing complex assembly, regulation of mononuclear cell migration were among the BPs we observed. Metallo-endopeptidase and peptidase activity was discovered to be the most common molecular functions in which they are involved (figure 6(4B)). Furthermore, we discovered their participation in the collagen-containing extracellular matrix, ficolin-1-rich granule membrane, and clathrin-coated vesicle cellular components (figure 6(4C)).

### **Functional enrichment analysis of gene targets of fortunellin in liver organoids**

ACHE, NRAS, IGFBP3, FGF2, ERAP2, CASP7, and CASP1 were employed as fortunellin gene targets in liver organoid functional enrichment analysis. Proteolysis, positive regulation of endothelial cell proliferation, regulation of endothelial cell proliferation, small GTPase mediated signal transduction, positive regulation of epithelial cell proliferation, Ras protein signal transduction, negative regulation of cell migration, glycerophospholipid biosynthetic process, positive regulation of cAMP, positive regulation of cAMP, positive regulation of cAMP, positive regulation of cAMP, positive regulation of cAMP, positive regulation of Various cysteine-type endopeptidase activity, Insulin-like growth factor I&II binding, and protein phosphatase activator activity were discovered to be involved in their molecular functions (figure 6(5B)). Furthermore, we discovered their participation in endoplasmic reticulum lumen, basement membrane, tertiary granule membrane, and intracellular organelle lumen cellular components (figure 6(5C)).

### **Functional enrichment analysis of gene targets of fortunellin in cornea organoids**

In cornea organoids, we used the 8 gene targets of fortunellin: IL6, CA12, CYP1B1, ABCC1, CYP19A1, FN1, ANPEP, and ADAM17. Myeloid leukocyte mediated immunity, regulation of leukocyte chemotaxis, positive regulation of vascular endothelial growth factor production, regulation of vascular endothelial growth factor production, positive regulation of leukocyte migration, estrogen metabolic process, positive regulation of receptor signalling pathway via STAT, positive regulation of receptor signalling pathway via JAK-STAT, cAMP signalling pathway, cAMP signalling pathway, cAMP signalling pathway, cAMP signaling pathway, Interleukin-6 receptor binding was shown to be the most important molecular function in which they are involved, with a p-value of 2.94E-06 (figure 6(6B)). Furthermore, their involvement in cellular components of the endoplasmic reticulum lumen and membrane, intracellular organelle lumen, platelet alpha granule & its lumen, and organelle bounding membrane (figure 6(6C)) was discovered

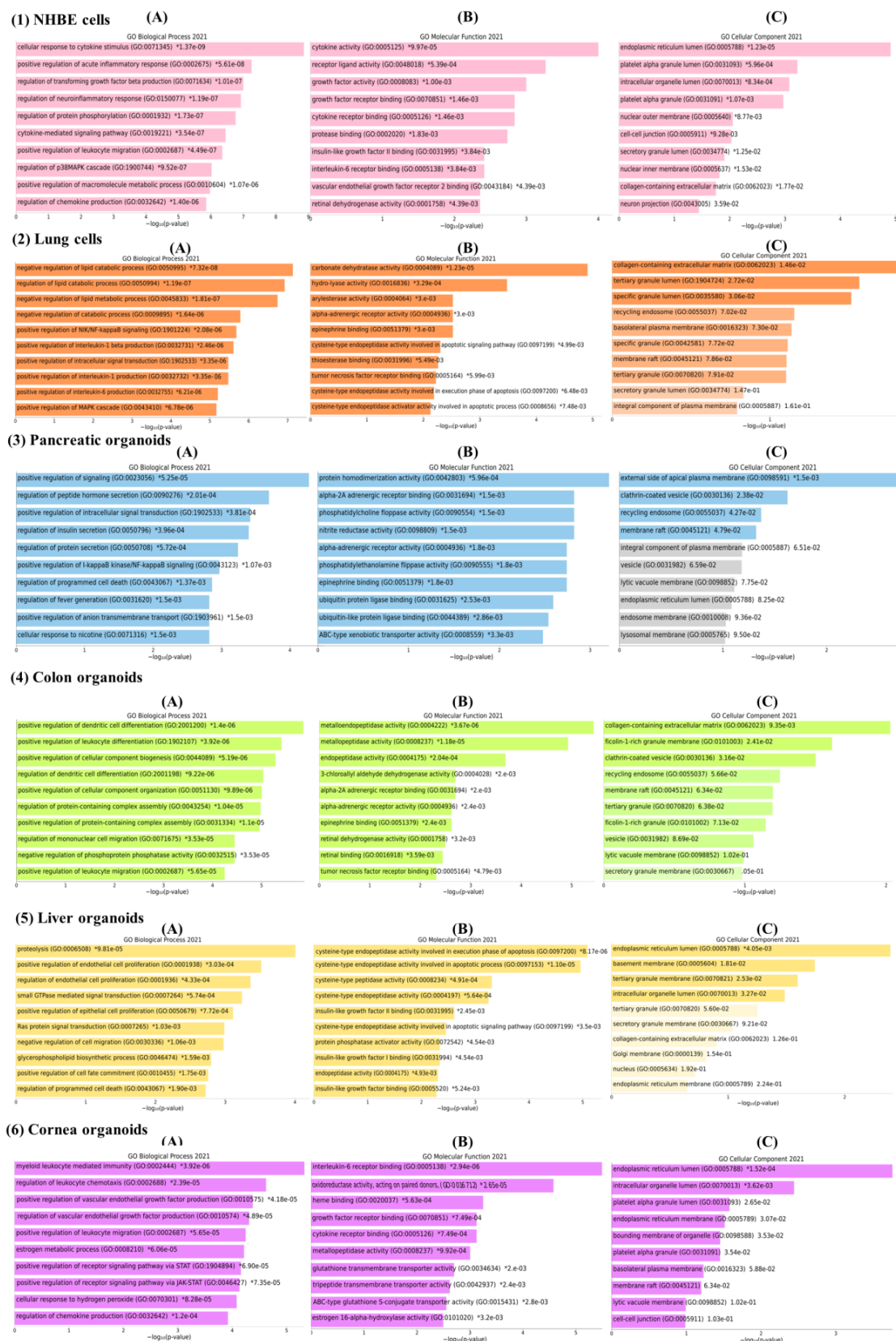


**Figure 6.** Functional enrichment analysis of upregulated genes targets of fortunellin in Covid-19 infected cells/organoids. The details of the genes of the GO terms are provided in Supplementary table S7 (A-F).

## **PPI, module detection and pathway enrichment analysis in NHBE cells, lung cells, pancreatic, colon, liver and cornea organoids**

In NHBE cells, we discovered that 28 of the 111 genes were upregulated. This network's module was statistically significant, with an MCODE score of 18.211, 20 nodes, and 173 edges (figure 7A). As network module hub genes and fortunellin targets, we found six key genes: VEGFA, TNF, IL6, FN1, PTGS2, and MMP1. The top five enriched pathways of the network modules' genes are shown in table 2. This highlighted fortunellin's significance in biological networks such as the TNF signaling system, the IL-17 signaling pathway, the AGE-RAGE signaling pathway in diabetic problems, the NF-kappa B signalling pathway, and the Relaxin signaling circuit. In lung cells, we found that 26 of the 110 genes were upregulated. With an MCODE score of 16.824, the observed module has 18 nodes and 143 edges. TNF, CASP1, and CD38 were identified as genes that were important to the module and were also targeted by Fortunellin. Among the processes linked with the module include influenza A, cytokine-cytokine receptor interaction, viral-protein interaction with cytokine and cytokine receptor, toll-like receptor signaling pathways, and neutrophil extracellular trap creation (table 2). In pancreatic organoids, 11 of the 106 genes were found to be elevated. With an MCODE score of 5.00, 5 nodes, and 10 edges, we discovered a statistically significant module. Furthermore, we discovered that Fortunellin targeted the TNF gene, which was critical to the module. The adipocytokine signaling route, insulin resistance, lipid and atherosclerosis, inflammatory bowel disease, and the AGE-RAGE signaling pathway in diabetic complications are among the pathways connected with the network module (table 2). We discovered that 26 of the 108 genes were elevated in colon organoids. With an MCODE score of 13.867, 16 nodes, and 104 edges, we discovered a statistically significant module. In addition, we identified three important genes, TNF, MMP1, and MMP7, that acted as a hub for the module and were also Fortunellin targets. The network module's linked pathways include rheumatoid arthritis, the IL-17 signalling route, the TNF signaling pathway, lipid and atherosclerosis, and the NF-kappa B signaling pathway, as illustrated in table 2.



We discovered that 11 of the 107 genes in liver organoids were activated. We discovered a major module with an MCODE score of 5.00, 5 nodes, and 10 edges. Furthermore, we discovered two critical genes, CASP1 and FGF2, that functioned as a hub for the module as well as Fortunellin targets. The top five pathways linked with the network module include influenza A, lipid and atherosclerosis, AGE-RAGE signaling pathway in diabetic complications, TNF signaling route, and NOD-like receptor signaling pathway (table 2). In cornea organoids, 12 of the 108 genes were identified to be overexpressed. With an MCODE score of 5.60, six nodes, and fourteen edges, a substantial module was discovered. Furthermore, we discovered three important genes, IL6, ANPEP, and FN1, that served as the module's hub and were Fortunellin targets. Fortunellin has been linked to a variety of biological pathways, including the hematopoietic cell lineage, the AGE-RAGE signaling route in diabetic complications, the PI3K-Akt signaling system, the ECM-receptor interaction, and the TNF signaling pathway.

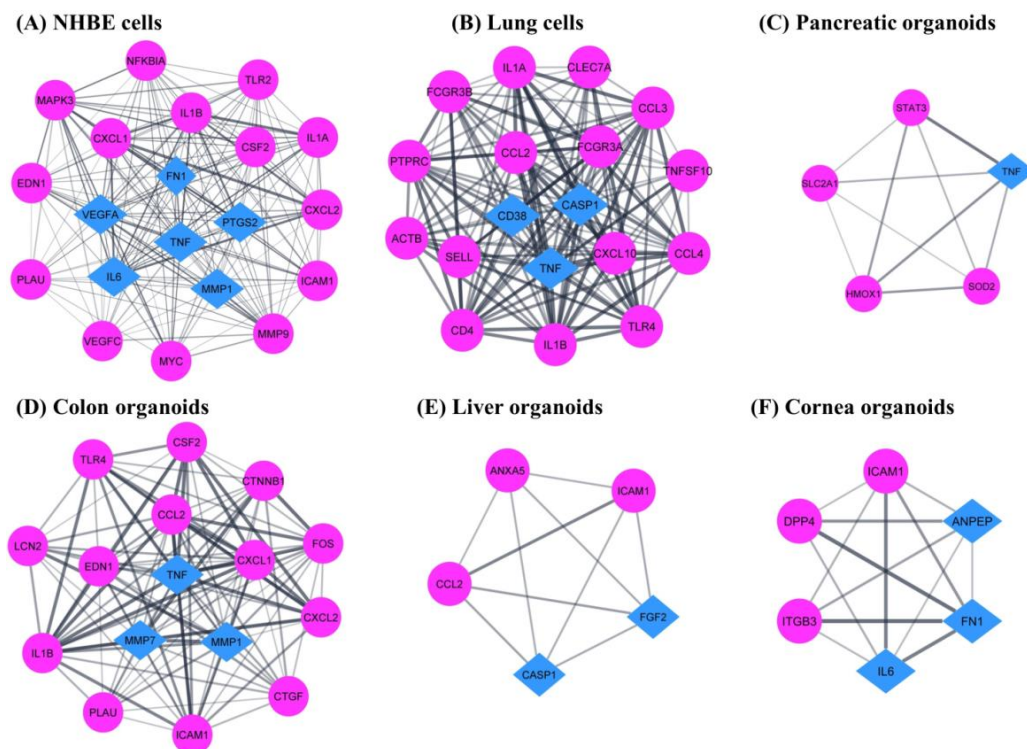


**Figure 7.** Modules and hub gene targets of fortunellin. Hub genes targeted by fortunellin in Covid-19 infected cells/organoids are shown in blue diamonds. The upregulated neighbors of the fortunellin targets are depicted in a pink circle.

**Table 2. Pathway enrichment analysis of network module's genes**

Term	Count	Genes	p-value
<b>NHBE cells</b>			
TNF signaling pathway	13	EDN1, CSF2, VEGFC, CXCL1, PTGS2, MMP9, CXCL2, TNF, ICAM1, NFKBIA, IL6, IL1B, MAPK3	1.94E-25
Rheumatoid arthritis	11	IL1A, IL6, CSF2, MMP1, IL1B, CXCL1, CXCL2, TNF, VEGFA, ICAM1, TLR2	1.93E-21
IL-17 signaling pathway	11	NFKBIA, IL6, CSF2, MMP1, IL1B, CXCL1, PTGS2, MMP9, CXCL2, TNF, MAPK3	2.19E-21
AGE-RAGE signaling pathway in diabetic complications	10	IL1A, EDN1, IL6, IL1B, FN1, VEGFC, TNF, VEGFA, ICAM1, MAPK3	1.09E-18
Lipid and atherosclerosis	11	NFKBIA, IL6, MMP1, IL1B, CXCL1, MMP9, CXCL2, TNF, ICAM1, MAPK3, TLR2	2.64E-17
<b>Lung Cells</b>			
Influenza A	9	IL1A, CXCL10, IL1B, TNFSF10, CASP1, CCL2, TNF, TLR4, ACTB	9.48E-15
Cytokine-cytokine receptor interaction	9	IL1A, CXCL10, CD4, IL1B, CCL4, TNFSF10, CCL3, CCL2, TNF	1.27E-12
Viral protein interaction with cytokine and cytokine receptor	6	CXCL10, CCL4, TNFSF10, CCL3, CCL2, TNF	2.37E-10
Toll-like receptor signaling pathway	6	CXCL10, IL1B, CCL4, CCL3, TNF, TLR4	3.01E-10
Neutrophil extracellular trap formation	6	FCGR3A, FCGR3B, CLEC7A, CASP1, TLR4, ACTB	1.11E-08
<b>Pancreatic organoids</b>			
Adipocytokinesignaling pathway	3	STAT3, SLC2A1, TNF	3.79E-05
Insulin resistance	3	STAT3, SLC2A1, TNF	5.05E-05
Lipid and atherosclerosis	3	STAT3, SOD2, TNF	2.92E-04
Inflammatory bowel disease	2	STAT3, TNF	0.002005
AGE-RAGE signaling pathway in diabetic complications	2	STAT3, TNF	0.003396
<b>Colon organoids</b>			
Rheumatoid arthritis	10	CSF2, MMP1, IL1B, CCL2, CXCL1, FOS, CXCL2, TNF, TLR4, ICAM1	2.24E-20
IL-17 signaling pathway	9	CSF2, MMP1, IL1B, LCN2, CCL2, CXCL1, FOS, CXCL2, TNF	8.40E-18
TNF signaling pathway	9	EDN1, CSF2, IL1B, CCL2, CXCL1, FOS, CXCL2, TNF, ICAM1	4.32E-17
Lipid and atherosclerosis	9	MMP1, IL1B, CCL2, CXCL1, FOS, CXCL2, TNF, TLR4, ICAM1	1.74E-14
NF-kappa B signaling pathway	7	PLAU, IL1B, CXCL1, CXCL2, TNF, TLR4, ICAM1	9.22E-13
<b>Liver organoids</b>			
Influenza A	3	CASP1, CCL2, ICAM1	6.17E-06
Lipid and atherosclerosis	3	CASP1, CCL2, ICAM1	1.21E-05
AGE-RAGE signaling pathway in diabetic complications	2	CCL2, ICAM1	2.45E-04
TNF signaling pathway	2	CCL2, ICAM1	3.07E-04
NOD-like receptor signaling pathway	2	CASP1, CCL2	8.00E-04
<b>Cornea organoids</b>			
Hematopoietic cell lineage	3	IL6, ANPEP, ITGB3	2.33E-06
AGE-RAGE signaling pathway in diabetic complications	3	IL6, FN1, ICAM1	2.40E-06
PI3K-Akt signaling pathway	3	IL6, ITGB3, FN1	1.06E-04
ECM-receptor interaction	2	ITGB3, FN1	2.84E-04
TNF signaling pathway	2	IL6, ICAM1	4.59E-04

## Discussion

Because of the high rate of replication, a SARS-CoV-2 infection generates more than one million virions in one day[51], and most known antivirals are ineffective against it due to SARS- CoV-2's inherent genetic mutability[61-63]. COVID-19 patients not only showed respiratory symptoms but also multi-organ dysfunction and inflammation [1, 2]. Therefore, In comparison to single target approaches, concurrent inhibition of multiple SARS-CoV-2 targets combined with inflammation and immunomodulation associated tissue-specific host targets may be more effective and have a significantly higher therapeutic potential in saving the life of a COVID-19 patient. In this study, we discovered that fortunellin, a naturally occurring flavonoid O-glycoside molecule, exhibits multi-targeting potential against key SARS-CoV-2 target proteins. We have also discovered the potential human targets of fortunellin in SARS-CoV-2 infected tissues including human NHBE cells, lung cells, pancreatic organoids, colon organoids, liver organoids, and cornea organoids.

Fortunellin which is one of the constituents of Gojihwadi Kwath, an Indian traditional-Ayurvedic formulation; is known to have antioxidant and ant-inflammatory biological properties in animals[64, 65] and can also be extracted from *Citrus japonica* var. *margarita* fruits[66]. Traditionally, the Gojihwadi Kwath is well known to have antiviral properties and has been used in COVID-19 treatment and management [18-21]. However, the mechanism of its antiviral activity remains unknown. It was recently found that fortunellin inhibits Mpro dimerization[60]. Fortunellin has also been shown to exhibit inhibitory activity against HIV-1 protease [67], as well as antibacterial properties [68]. Furthermore, Fortunellin's pharmacodynamic–pharmacokinetic properties show that it is water-soluble with low absorption in the GI tract; fortunellin is non-toxic because it does not interact with the CYPs involved in drug metabolism; and fortunellin is a substrate of the P-glycoprotein 1 (Pgp or MDR1) multidrug transporter, implying rapid elimination from the body (Supplementary table S3 and S4 ) [60]. As an outcome, the application of Fortunellin's multi-target potentials for the therapy of COVID-19 could be promising. This prompted us to examine the effect

of fortunellin on the key targets of SARS CoV-2, including Mpro, PLpro, RdRp, NendoU, replicase (monomer and dimer forms), Helicase, 2'O-methyltransferase, S-RBD, N-NTD, and N-CTD, all of which are considered necessary for viral replication, growth, invasion, and infectivity. The negative binding energies (figure 1 and Supplementary table S2) allowed us to propose that fortunellin may act as a potential multi-target drug against Covid-19. Additionally, to validate the reliability and interaction stability of the docked complexes, we performed 100ns long MD simulations of each of the twelve fortunellin-target complexes that resulted in a total of 1.2  $\mu$ s long molecular trajectories. We found that all the complexes were stable throughout the run as indicated by their steady RMSD value, and low and stable Rg values. Also, the minimum distance between the fortunellin-target complexes was stably maintained, indicating that the ligand was in close proximity of the receptor throughout 100 ns. A stable residue fluctuation (RMSF value) of the residues of ligand binding site in all the fortunellin-target complexes suggests that the favorable accommodation of fortunellin. Next, through MD simulation, we intended to evaluate the binding affinity of the fortunellin–target complexes and identified the key residues contributing to their affinity. We validated and computed the binding free energy of the ligand–target complexes using MM-GBSA. The MM/GBSA approach has been widely used to examine the receptor-ligand interaction [36]. 1000 snapshots extracted at every 3 ps of intervals from the last 30 ns MD trajectory, was used for the MM-GBSA calculations. The negative binding free energy, which ranges from -51 to -14 kcal/mol, indicates that fortunellin-target complexes are stable including N-CTD (-51.30 kcal/mol) and Replicase-dimer (-45.91 kcal/mol) at the top of the list, followed by Replicase (monomer)- NSP-8 binding site (-29.9 kcal/mol), PLpro (-29.60 kcal/mol), 2'-O-methyltransferase (-24.33 kcal/mol), Mpro (-23.48 kcal/mol), Spike-RBD (-23.3 kcal/mol), Replicase (monomer) at dimer interface (-21.03 kcal/mol), NendoU (-16.83 kcal/mol) and RdRp (-14.24 kcal/mol) (table 1). We decomposed the binding energy  $\Delta G_{\text{MM-GBSA}}$  by residue to get a more precise thermodynamic description of the residue contributions. The decomposition method helped identify residues involved in receptor-ligand

interactions. Masking these residues via fortunelling may prevent them to participate in their molecular functions.

Next, we employed the network pharmacology strategy to reveal the effect of fortunellin on the host system as an inhibitor of the upregulated genes responsible for excess inflammation and failure of immune responses. The role of fortunellin was explored in normal human bronchial epithelial cells, lung cells, and pancreatic, colon, liver, and cornea organoids. We have noted that in the SARS-CoV-2 infected six tissues, 36 genes were upregulated and targeted by fortunellin including ABCB1, ABCC1, ACHE, ADAM17, ADRA2A, ADRA2C, AKR1B1, ALDH1A2, ANPEP, CA1, CA12, CASP1, CASP7, CBS, CD38, CYP19A1, CYP1B1, ECE1, EPHA2, ERAP2, FGF2, FN1, HCAR2, IGFBP3, IL6, LGALS1, LGALS3, LGALS9, MMP1, MMP7, MMP8, NRAS, PTGS2, TNF, VEGFA, and XDH. Among them, we have found that a total of 11 upregulated genes i.e., TNF, IL6, ANPEP, CASP1, CD38, FGF2, FN1, MMP1, MMP7, PTGS2, and VEGFA were associated with functionally important modules (figure 7). The involvement of these genes in a variety of biologically important pathways, including anti-inflammatory, immunomodulatory, and apoptotic pathways, suggests that fortunellin plays a protective role in the host system. The TNF and IL6 genes encode for proteins involved in the regulation of inflammatory processes. It has been observed that serum TNF- $\alpha$  [69] and IL6 [70] levels are elevated in patients with COVID-19 and are higher with more severe diseases. We noticed that elevated expression of TNF is associated with normal human bronchial epithelial cells, lung cells and pancreatic, and colon organoids. Cell surface protein ANPEP (anaryl aminopeptidase membrane), the target of fortunellin, has been reported to promote SARS-CoV-2 entry into target cells[71]. Inflammasome activation was observed in COVID-19 patients' peripheral immune cells and tissues, and the level of inflammasome-derived products, including active caspase-1, was associated with disease severity and poor outcomes. [72]. Horenstein et al. showed that CD38 plays a central role in altered immunometabolism resulting from COVID-19 infection and may be a promising therapeutic target of fortunellin [73]. The hyper-expression of FGF2 could be implicated in the pathogenesis of coronavirus infections by inducing apoptosis[74].

Therefore inhibiting its signaling, might represent a promising target of fortunellin[75]. Alveolar M2 macrophages produce fibro-proliferative markers, such as MMP7 which promote fibrogenesis leading to lung stiffening; thus, its elevated expression are more vulnerable to COVID-19 infections[76, 77]. Plasma MMP-1 enzymatic activity and plasma levels of MMP-1 and VEGF-A were significantly elevated in critical COVID-19 patients [78]. Excessive expression of MMP-1 plays a central role in tissue destruction in a wide variety of vascular diseases. Elevated VEGF-A, an endothelial cells (EC) activation marker, increases vascular permeability [79]. Excessive MMP-1 and hyperactivation of ECs occur in COVID-19 patients and are associated with the severity of COVID-19. Prostaglandin-endoperoxide synthase 2 (*PTGS2*) or Cyclo-oxygenase2 (Cox-2) is an inducible pro-inflammatory enzyme required for efficient entry and RNA replication[80]. An effective COX-2 inhibitor during early viral infection may enhance and/or prolong endogenous interferon responses, and thereby might increase anti-viral immunity[81]. Thus, the elevated TNF, IL6, ANPEP, CASP1, CD38, FGF2, FN1, MMP1, MMP7, PTGS2, and VEGFA could be promising therapeutic targets of fortunellin. In the future, fortunellin can undergo further investigations in vitro and in vivo to unravel its antiviral action against COVID-19 treatment. The use of phytochemical fortunellin could be promising to minimize the side effect(s) which is otherwise caused by the use of synthetic drug molecules.

## Conclusion

Our findings show that fortunellin has a dual role; antiviral activities against SARS-CoV-2, and anti-inflammatory-Immunomodulatory capabilities against the host. Molecular Docking studies provided us with the preliminary idea of inhibitory action of fortunellin on the key targets of the SARS-CoV-2. The stability of the docked complexes was validated by the molecular dynamics simulations. The results from the energy calculations through MM-GBSA technique clearly indicated the extent of interaction between the catalytically important residues of each protein with fortunellin thus masking of these residues makes them unavailable to participate in their functions. Furthermore, network pharmacology analysis revealed that the elevated TNF, IL6, ANPEP, CASP1, CD38, FGF2, FN1, MMP1, MMP7, PTGS2, and VEGFA could be a promising therapeutic target of fortunellin on the host system. Fortunellin is a promising candidate for preventing and treating COVID-19 and SARS by supporting protective immunity while inhibiting pro-inflammatory cytokines, inhibiting viral infection and replication, inducing apoptosis, and protecting against tissue damage. Given fortunellin oral bioavailability and safety, the current study could lead to the development of fortunellin as an orally active COVID-19 and SARS therapeutic.

## Highlights

- Fortunellin reliably binds to and masks the 12 active pockets of nine targets of the SARS-CoV-2
- Main Protease, PLpro, RdRp, NendoU, Replicase (monomer and dimer forms), Helicase, and 2'O-methyltransferase are among the enzymes that fortunellin targets
- Fortunellin targets structural proteins that are required for viral replication, growth, invasion, and infectivity, such as Spike-RBD, Nucleocapsid-NTD, and Nucleocapsid-CTD
- Fortunellin showed the highest affinity for the Nucleocapsid (N-CTD) domain (-51.30 kcal/mol) and Replicase-dimer (-45.91 kcal/mol)
- Fortunellin may target TNF, IL6, ANPEP, CASP1, CD38, FGF2, FN1, MMP1, MMP7, PTGS2, and VEGFA of host and could be a promising therapeutic target.



### **Author contributions statement**

R.M and E.P. conceived, designed, and supervised the whole study of the research. Docking studies were performed by S.A and V.M; Molecular Dynamics was performed by S.A and A.P. Energy calculations and analysis was performed by E.P. S.A performed literature survey and prepared the illustrations; SA., and RM analyzed data; SA. E.P and R.M wrote the manuscript. S.K.M.; P.S.B, S.D, A.K.C, V.M.S., R.N.C., and N.A. contributed to various aspects of the work. All authors have read and agreed to the published version of the manuscript.

### **Acknowledgements**

Vibha Mishra is supported with a Research Fellowship from the BHU. Afifa Parveen is supported with CSIR-SRF, Govt. of India. Research support from the IoE, Banaras Hindu University is gratefully acknowledged. We also acknowledge National medicos organisation, Gau sewa Sewa Bharti, Rastriya Kamdhenu Ayog, Lok Aayurved, Arogya Bharti, Vishwa Ayurved Parisad. We acknowledge Prof. A. K Tripathi, Director, Institute of Science, BHU, and Prof. Inu Mehta, MMV, BHU for their support.

### **Declaration of competing interest**

The authors declare that there are no conflicts of interest with the contents of this article.

## References

- [1] A. Gupta, M.V. Madhavan, K. Sehgal, N. Nair, S. Mahajan, T.S. Sehrawat, B. Bikdeli, N. Ahluwalia, J.C. Ausiello, E.Y. Wan, Extrapulmonary manifestations of COVID-19, *Nature medicine*, 26 (2020) 1017-1032.
- [2] X. Yao, T. Li, Z. He, Y. Ping, H. Liu, S. Yu, H. Mou, L. Wang, H. Zhang, W. Fu, A pathological report of three COVID-19 cases by minimally invasive autopsies, *Zhonghua bing li xue za zhi= Chinese journal of pathology*, 49 (2020) E009-E009.
- [3] D. Brian, R.J.C.r. Baric, r. genetics, Coronavirus genome structure and replication, (2005) 1-30.
- [4] M.Z. Tay, C.M. Poh, L. Rénia, P.A. MacAry, L.F.J.N.R.I. Ng, The trinity of COVID-19: immunity, inflammation and intervention, 20 (2020) 363-374.
- [5] K. Anand, G.J. Palm, J.R. Mesters, S.G. Siddell, J. Ziebuhr, R. Hilgenfeld, Structure of coronavirus main proteinase reveals combination of a chymotrypsin fold with an extra  $\alpha$ -helical domain, *The EMBO journal*, 21 (2002) 3213-3224.
- [6] H. Yang, M. Yang, Y. Ding, Y. Liu, Z. Lou, Z. Zhou, L. Sun, L. Mo, S. Ye, H. Pang, The crystal structures of severe acute respiratory syndrome virus main protease and its complex with an inhibitor, *Proceedings of the National Academy of Sciences*, 100 (2003) 13190-13195.
- [7] J. Ziebuhr, E.J. Snijder, A.E. Gorbalenya, Virus-encoded proteinases and proteolytic processing in the Nidovirales, *Microbiology*, 81 (2000) 853-879.
- [8] X. Deng, Y. Chen, A.M. Mielech, M. Hackbart, K.R. Kesely, R.C. Mettelman, A. O'Brien, M.E. Chapman, A.D. Mesecar, S.C. Baker, Structure-guided mutagenesis alters deubiquitinating activity and attenuates pathogenesis of a murine coronavirus, *Journal of virology*, 94 (2020) e01734-01719.
- [9] W. Rut, Z. Lv, M. Zmudzinski, S. Patchett, D. Nayak, S.J. Snipas, F. El Oualid, T.T. Huang, M. Bekes, M. Drag, Activity profiling and crystal structures of inhibitor-bound SARS-CoV-2 papain-like protease: A framework for anti-COVID-19 drug design, *Science advances*, 6 (2020) eabd4596.
- [10] E.J. Snijder, E. Decroly, J. Ziebuhr, The Nonstructural Proteins Directing Coronavirus RNA Synthesis and Processing, *Adv Virus Res*, 96 (2016) 59-126.
- [11] J. Ziebuhr, E.J. Snijder, A.E. Gorbalenya, Virus-encoded proteinases and proteolytic processing in the Nidovirales, *J Gen Virol*, 81 (2000) 853-879.
- [12] Y. Chen, Q. Liu, D.J.J.o.m.v. Guo, Emerging coronaviruses: genome structure, replication, and pathogenesis, *J Journal of medical virology*, 92 (2020) 418-423.
- [13] T. Shu, M. Huang, D. Wu, Y. Ren, X. Zhang, Y. Han, J. Mu, R. Wang, Y. Qiu, D.-Y. Zhang, SARS-coronavirus-2 Nsp13 possesses NTPase and RNA helicase activities that can be inhibited by bismuth salts, *Virologica Sinica*, 35 (2020) 321-329.
- [14] Y. Chen, D. Guo, Molecular mechanisms of coronavirus RNA capping and methylation, *Virol Sin*, 31 (2016) 3-11.
- [15] A.C. Walls, Y.-J. Park, M.A. Tortorici, A. Wall, A.T. McGuire, D. Veisler, Structure, function, and antigenicity of the SARS-CoV-2 spike glycoprotein, *Cell*, 181 (2020) 281-292. e286.
- [16] M. Hoffmann, H. Kleine-Weber, S. Pöhlmann, A multibasic cleavage site in the spike protein of SARS-CoV-2 is essential for infection of human lung cells, *Molecular cell*, 78 (2020) 779-784. e775.
- [17] Y. Cong, M. Ulasli, H. Schepers, M. Mauthe, P. V'kovski, F. Kriegenburg, V. Thiel, C.A. de Haan, F. Reggiori, Nucleocapsid protein recruitment to replication-transcription complexes plays a crucial role in coronaviral life cycle, *Journal of virology*, 94 (2020) e01925-01919.
- [18] G.C. Pamnani, P. Vardhan, R.K. Soni, Management approach to Covid-19 associated upper respiratory tract infection in Ayurveda: A review study, *Journal of Ayurveda*, 14 (2020) 49.
- [19] P.A. Jyothi, A. Dileep, D. Devarajan, A. Sharma, S. Kumari, S. Rathuri, S. Rai, P. Dharmarajan, T.M. Nesari, Three case reports of moderate COVID-19 infection managed through Ayurvedic approach, *Journal of Ayurveda Case Reports*, 3 (2020) 84.
- [20] K. Chambyal, S. Sharma, S. Sharma, Ayurveda prophylaxis and intervention for COVID-19 Pandemic, *J Journal of Ayurveda*, 14 (2020) 22.

- [21] S. Kumar, Ayurveda interpretation, diagnostic, and probable management of COVID-19 pandemic, *Journal of Indian System of Medicine*, 8(2020) 91.
- [22] H.M. Berman, J. Westbrook, Z. Feng, G. Gilliland, T.N. Bhat, H. Weissig, I.N. Shindyalov, P.E.J.N.a.r. Bourne, The protein data bank, 28 (2000) 235-242.
- [23] E.F. Pettersen, T.D. Goddard, C.C. Huang, G.S. Couch, D.M. Greenblatt, E.C. Meng, T.E. Ferrin, UCSF Chimera—a visualization system for exploratory research and analysis, *Journal of computational chemistry*, 25 (2004) 1605-1612.
- [24] S. Kim, J. Chen, T. Cheng, A. Gindulyte, J. He, S. He, Q. Li, B.A. Shoemaker, P.A. Thiessen, B. Yu, PubChem 2019 update: improved access to chemical data, *Nucleic acids research*, 47 (2019) D1102-D1109.
- [25] N.M. O'Boyle, M. Banck, C.A. James, C. Morley, T. Vandermeersch, G.R. Hutchison, Open Babel: An open chemical toolbox, *Journal of cheminformatics*, 3 (2011) 1-14.
- [26] O. Trott, A.J. Olson, AutoDock Vina: improving the speed and accuracy of docking with a new scoring function, efficient optimization, and multithreading, *Journal of computational chemistry*, 31 (2010) 455-461.
- [27] M.J. Abraham, T. Murtola, R. Schulz, S. Páll, J.C. Smith, B. Hess, E.J.S. Lindahl, GROMACS: High performance molecular simulations through multi-level parallelism from laptops to supercomputers, 1 (2015) 19-25.
- [28] J. Huang, S. Rauscher, G. Nawrocki, T. Ran, M. Feig, B.L. de Groot, H. Grubmuller, A.D. MacKerell, Jr., CHARMM36m: an improved force field for folded and intrinsically disordered proteins, *Nat Methods*, 14 (2017) 71-73.
- [29] V. Zoete, M.A. Cuendet, A. Grosdidier, O. Michielin, SwissParam: a fast force field generation tool for small organic molecules, *J Comput Chem*, 32 (2011) 2359-2368.
- [30] T. Darden, D. York, L. Pedersen, Particle mesh Ewald: An  $N \cdot \log(N)$  method for Ewald sums in large systems, *The Journal of chemical physics*, 98 (1993) 10089-10092.
- [31] B. Hess, H. Bekker, H.J. Berendsen, J.G. Fraaije, LINCS: a linear constraint solver for molecular simulations, *Journal of computational chemistry*, 18 (1997) 1463-1472.
- [32] G. Bussi, D. Donadio, M. Parrinello, Canonical sampling through velocity rescaling, *The Journal of chemical physics*, 126 (2007) 014101.
- [33] M. Parrinello, A. Rahman, Polymorphic transitions in single crystals: A new molecular dynamics method, *Journal of Applied physics*, 52 (1981) 7182-7190.
- [34] W.F. Van Gunsteren, H.J. Berendsen, A leap-frog algorithm for stochastic dynamics, *Molecular Simulation*, 1 (1988) 173-185.
- [35] P. Turner, XMGRACE, Version 5.1. 19, Center for Coastal and Land-Margin Research, Oregon Graduate Institute of Science and Technology, Beaverton, OR, 2 (2005).
- [36] S. Genheden, U. Ryde, The MM/PBSA and MM/GBSA methods to estimate ligand-binding affinities, *Expert Opin Drug Discov*, 10 (2015) 449-461.
- [37] D.A. Case, H.M. Aktulga, K. Belfon, I. Ben-Shalom, S.R. Brozell, D. Cerutti, T. Cheatham, V.W.D. Cruzeiro, T. Darden, R.E. Duke, Amber 2021: Reference Manual, (2021).
- [38] B.R. Miller III, T.D. McGee Jr, J.M. Swails, N. Homeyer, H. Gohlke, A.E. Roitberg, MMPBSA.py: an efficient program for end-state free energy calculations, *Journal of chemical theory computation*, 8(2012) 3314-3321.
- [39] M.S. Valdés-Tresanco, M.E. Valdés-Tresanco, P.A. Valiente, E.J.J.o.C.T. Moreno, Computation, gmx\_MMPBSA: A New Tool to Perform End-State Free Energy Calculations with GROMACS, *Journal of Chemical Theory Computation*, (2021).
- [40] J.A. Maier, C. Martinez, K. Kasavajhala, L. Wickstrom, K.E. Hauser, C. Simmerling, ff14SB: Improving the Accuracy of Protein Side Chain and Backbone Parameters from ff99SB, *J Chem Theory Comput*, 11 (2015) 3696-3713.

- [41] J. Wang, R.M. Wolf, J.W. Caldwell, P.A. Kollman, D.A. Case, Development and testing of a general amber force field, *J Comput Chem*, 25 (2004) 1157-1174.
- [42] A. Jakalian, D.B. Jack, C.I. Bayly, Fast, efficient generation of high-quality atomic charges. AM1-BCC model: II. Parameterization and validation, *J Comput Chem*, 23 (2002) 1623-1641.
- [43] G. Xiong, Z. Wu, J. Yi, L. Fu, Z. Yang, C. Hsieh, M. Yin, X. Zeng, C. Wu, A. Lu, ADMETLab 2.0: an integrated online platform for accurate and comprehensive predictions of ADMET properties, *Nucleic Acids Research*, 49 (2021) W5-W14.
- [44] D.E. Pires, T.L. Blundell, D.B. Ascher, pkCSM: predicting small-molecule pharmacokinetic and toxicity properties using graph-based signatures, *Journal of medicinal chemistry*, 58 (2015) 4066-4072.
- [45] M.J. Keiser, B.L. Roth, B.N. Armbruster, P. Ernsberger, J.J. Irwin, B.K. Shoichet, Relating protein pharmacology by ligand chemistry, *Nat Biotechnol*, 25 (2007) 197-206.
- [46] D. Gfeller, A. Grosdidier, M. Wirth, A. Daina, O. Michielin, V. Zoete, SwissTargetPrediction: a web server for target prediction of bioactive small molecules, *Nucleic Acids Res*, 42 (2014) W32-38.
- [47] M.V. Kuleshov, M.R. Jones, A.D. Rouillard, N.F. Fernandez, Q. Duan, Z. Wang, S. Koplev, S.L. Jenkins, K.M. Jagodnik, A. Lachmann, M.G. McDermott, C.D. Monteiro, G.W. Gundersen, A. Ma'ayan, Enrichr: a comprehensive gene set enrichment analysis web server 2016 update, *Nucleic Acids Res*, 44 (2016) W90-97.
- [48] N.T. Doncheva, J.H. Morris, J. Gorodkin, L.J. Jensen, Cytoscape StringApp: Network Analysis and Visualization of Proteomics Data, *J Proteome Res*, 18 (2019) 623-632.
- [49] W.P. Bandettini, P. Kellman, C. Mancini, O.J. Booker, S. Vasu, S.W. Leung, J.R. Wilson, S.M. Shanbhag, M.Y. Chen, A.E. Arai, MultiContrast Delayed Enhancement (MCOE) improves detection of subendocardial myocardial infarction by late gadolinium enhancement cardiovascular magnetic resonance: a clinical validation study, *J Cardiovasc Magn Reson*, 14 (2012) 83.
- [50] S.-H. Chen, C.-H. Chin, H.-H. Wu, C.-W. Ho, M.-T. Ko, C.-Y. Lin, cyto-Hubba: A Cytoscape plug-in for hub object analysis in network biology, 20th International Conference on Genome Informatics, Citeseer, 2009.
- [51] M. Kanehisa, S. Goto, KEGG: kyoto encyclopedia of genes and genomes, *Nucleic Acids Res*, 28 (2000) 27-30.
- [52] D.W. Kneller, G. Phillips, H.M. O'Neill, R. Jedrzejczak, L. Stols, P. Langan, A. Joachimiak, L. Coates, A. Kovalevsky, Structural plasticity of SARS-CoV-2 3CL M pro active site cavity revealed by room temperature X-ray crystallography, *Nature communications*, 11 (2020) 1-6.
- [53] K. Świderek, V. Moliner, Revealing the molecular mechanisms of proteolysis of SARS-CoV-2 M pro by QM/MM computational methods, *Chemical Science*, 11 (2020) 10626-10630.
- [54] Y.L. Weng, S.R. Naik, N. Dingelstad, M.R. Lugo, S. Kalyaanamoorthy, A. Ganesan, Molecular dynamics and in silico mutagenesis on the reversible inhibitor-bound SARS-CoV-2 main protease complexes reveal the role of lateral pocket in enhancing the ligand affinity, *Sci Rep*, 11 (2021) 7429.
- [55] T.S. Komatsu, N. Okimoto, Y.M. Koyama, Y. Hirano, G. Morimoto, Y. Ohno, M. Taiji, Drug binding dynamics of the dimeric SARS-CoV-2 main protease, determined by molecular dynamics simulation, *Sci Rep*, 10 (2020) 16986.
- [56] A. Shitrit, D. Zaidman, O. Kalid, I. Bloch, D. Doron, T. Yarnizky, I. Buch, I. Segev, E. Ben-Zeev, E. Segev, O. Kobiler, Conserved interactions required for inhibition of the main protease of severe acute respiratory syndrome coronavirus 2 (SARS-CoV-2), *Sci Rep*, 10 (2020) 20808.
- [57] Z.J. Miknis, E.F. Donaldson, T.C. Umland, R.A. Rimmer, R.S. Baric, L.W. Schultz, Severe acute respiratory syndrome coronavirus nsp9 dimerization is essential for efficient viral growth, *Journal of virology*, 83 (2009) 3007-3018.
- [58] A.R. Collins, R.L. Knobler, H. Powell, M.J.J.V. Buchmeier, Monoclonal antibodies to murine hepatitis virus-4 (strain JHM) define the viral glycoprotein responsible for attachment and cell-cell fusion, 119 (1982) 358-371.
- [59] A.C. Walls, Y.-J. Park, M.A. Tortorici, A. Wall, A.T. McGuire, D.J.C. Veasler, Structure, function, and antigenicity of the SARS-CoV-2 spike glycoprotein, 181 (2020) 281-292. e286.

- [60] A.A. Panagiotopoulos, I. Karakasiliotis, D.M. Kotzampasi, M. Dimitriou, G. Sourvinos, M. Kampa, S. Pirintzos, E. Castanas, V. Daskalakis, Natural Polyphenols Inhibit the Dimerization of the SARS-CoV-2 Main Protease: The Case of Fortunellin and Its Structural Analogs, *Molecules*, 26 (2021) 6068.
- [61] E. Callaway, Heavily mutated Omicron variant puts scientists on alert, *Nature*, 600 (2021) 21.
- [62] S. Poudel, A. Ishak, J. Perez-Fernandez, E. Garcia, D.A. León-Figueroa, L. Romaní, D.K. Bonilla-Aldana, A.J. Rodriguez-Morales, Highly mutated SARS-CoV-2 Omicron variant sparks significant concern among global experts—What is known so far?, *Travel medicine infectious disease*, 45 (2022) 102234.
- [63] Y.L. Ng, C.K. Salim, J.J.H. Chu, Drug repurposing for COVID-19: Approaches, challenges and promising candidates, *Pharmacol Ther*, 228 (2021) 107930.
- [64] C. Zhao, Y. Zhang, H. Liu, P. Li, H. Zhang, G. Cheng, Fortunellin protects against high fructose-induced diabetic heart injury in mice by suppressing inflammation and oxidative stress via AMPK/Nrf-2 pathway regulation, *Biochem Biophys Res Commun*, 490 (2017) 552-559.
- [65] Y. Xiong, J. Qiu, C. Li, Y. Qiu, L. Guo, Y. Liu, J. Wan, Y. Li, G. Wu, L. Wang, Z. Zhou, J. Dong, C. Du, D. Chen, H. Guo, Fortunellin-Induced Modulation of Phosphatase and Tensin Homolog by MicroRNA-374a Decreases Inflammation and Maintains Intestinal Barrier Function in Colitis, *Front Immunol*, 9 (2018) 83.
- [66] S.N. Lou, Y.C. Lai, Y.S. Hsu, C.T. Ho, Phenolic content, antioxidant activity and effective compounds of kumquat extracted by different solvents, *Food Chem*, 197 (2016) 1-6.
- [67] H.X. Xu, M. Wan, H. Dong, P.P. But, L.Y. Foo, Inhibitory activity of flavonoids and tannins against HIV-1 protease, *Biol Pharm Bull*, 23 (2000) 1072-1076.
- [68] W. Rizvi, M. Rizvi, R. Kumar, A. Kumar, I. Shukla, M. Parveen, Antibacterial activity of *Ficus lyrata*-An in vitro study, *Int. J. Pharmacol*, 8 (2010) 7.
- [69] E. Mortaz, P. Tabarsi, H. Jamaati, N.D. Roofchayee, N.K. Dezfouli, S.M. Hashemian, A. Moniri, M. Marjani, M. Malekmohammad, D. Mansouri, Increased Serum Levels of Soluble TNF- $\alpha$  Receptor Is Associated With ICU Mortality in COVID-19 Patients, *Frontiers in Immunology*, 12 (2021).
- [70] D.M. Del Valle, S. Kim-Schulze, H.H. Huang, N.D. Beckmann, S. Nirenberg, B. Wang, Y. Lavin, T.H. Swartz, D. Madduri, A. Stock, T.U. Marron, H. Xie, M. Patel, K. Tuballes, O. Van Oekelen, A. Rahman, P. Kovatch, J.A. Aberg, E. Schadt, S. Jagannath, M. Mazumdar, A.W. Charney, A. Firpo-Betancourt, D.R. Mendu, J. Jhang, D. Reich, K. Sigel, C. Cordon-Cardo, M. Feldmann, S. Parekh, M. Merad, S. Gnjatic, An inflammatory cytokine signature predicts COVID-19 severity and survival, *Nat Med*, 26 (2020) 1636-1643.
- [71] M. Letko, A. Marzi, V. Munster, Functional assessment of cell entry and receptor usage for SARS-CoV-2 and other lineage B betacoronaviruses, *Nat Microbiol*, 5 (2020) 562-569.
- [72] T.S. Rodrigues, K.S.G. de Sa, A.Y. Ishimoto, A. Becerra, S. Oliveira, L. Almeida, A.V. Goncalves, D.B. Perucello, W.A. Andrade, R. Castro, F.P. Veras, J.E. Toller-Kawahisa, D.C. Nascimento, M.H.F. de Lima, C.M.S. Silva, D.B. Caetite, R.B. Martins, I.A. Castro, M.C. Pontelli, F.C. de Barros, N.B. do Amaral, M.C. Giannini, L.P. Bonjorno, M.I.F. Lopes, R.C. Santana, F.C. Vilar, M. Auxiliadora-Martins, R. Luppino-Assad, S.C.L. de Almeida, F.R. de Oliveira, S.S. Batah, L. Siyuan, M.N. Benatti, T.M. Cunha, J.C. Alves-Filho, F.Q. Cunha, L.D. Cunha, F.G. Frantz, T. Kohlsdorf, A.T. Fabro, E. Arruda, R.D.R. de Oliveira, P. Louzada-Junior, D.S. Zamboni, Inflammasomes are activated in response to SARS-CoV-2 infection and are associated with COVID-19 severity in patients, *J Exp Med*, 218 (2021).
- [73] A.L. Horenstein, A.C. Faini, F. Malavasi, CD38 in the age of COVID-19: a medical perspective, *Physiol Rev*, 101 (2021) 1457-1486.
- [74] M.L. Yeung, Y. Yao, L. Jia, J.F. Chan, K.H. Chan, K.F. Cheung, H. Chen, V.K. Poon, A.K. Tsang, K.K. To, M.K. Yiu, J.L. Teng, H. Chu, J. Zhou, Q. Zhang, W. Deng, S.K. Lau, J.Y. Lau, P.C. Woo, T.M. Chan, S. Yung, B.J. Zheng, D.Y. Jin, P.W. Mathieson, C. Qin, K.Y. Yuen, MERS

- coronavirus induces apoptosis in kidney and lung by upregulating Smad7 and FGF2, *Nat Microbiol*, 1 (2016) 16004.
- [75] S. Meini, T. Giani, C. Tascini, Intussusceptive angiogenesis in Covid-19: hypothesis on the significance and focus on the possible role of FGF2, *Mol Biol Rep*, 47 (2020) 8301-8304.
- [76] A.S.M. Moin, T. Sathyapalan, S.L. Atkin, A.E. Butler, Pro-fibrotic M2 macrophage markers may increase the risk for COVID19 in type 2 diabetes with obesity, *Metabolism*, 112 (2020) 154374.
- [77] A.N. El-Din, K.A.E.-S. Ata, A.R. Abdel-Gawad, N.F. Fahmy, Impact of High Serum Levels of MMP-7, MMP-9, TGF- $\beta$  and PDGF Macrophage Activation Markers on Severity of COVID-19 in Obese-Diabetic Patients, *J Infection Drug Resistance*, 14 (2021) 4015.
- [78] F. Syed, W. Li, R.F. Relich, P.M. Russell, S. Zhang, M.K. Zimmerman, Q. Yu, Excessive matrix metalloproteinase-1 and hyperactivation of endothelial cells occurred in COVID-19 patients and were associated with the severity of COVID-19, *The Journal of infectious diseases*, (2021).
- [79] M. McMahon, S. Ye, J. Pedrina, D. Dlugolenski, J. Stambas, Extracellular Matrix Enzymes and Immune Cell Biology, *Front Mol Biosci*, 8 (2021) 703868.
- [80] M. Raaben, A.W. Einerhand, L.J. Taminiau, M. Van Houdt, J. Bouma, R.H. Raatgeep, H.A. Büller, C.A. De Haan, J.W. Rossen, Cyclooxygenase activity is important for efficient replication of mouse hepatitis virus at an early stage of infection, *Virology journal*, 4(2007) 1-5.
- [81] P. Prasher, M. Sharma, R. Gunupuru, Targeting cyclooxygenase enzyme for the adjuvant COVID-19 therapy, *Drug Dev Res*, 82 (2021) 469-473.